



OPEN

Computational prognostic evaluation of Alzheimer's drugs from FDA-approved database through structural conformational dynamics and drug repositioning approaches

Mubashir Hassan¹, Saba Shahzadi¹, Muhammad Yasir², Wanjoo Chun² & Andrzej Kloczkowski^{1,3}

Drug designing is high-priced and time taking process with low success rate. To overcome this obligation, computational drug repositioning technique is being promptly used to predict the possible therapeutic effects of FDA approved drugs against multiple diseases. In this computational study, protein modeling, shape-based screening, molecular docking, pharmacogenomics, and molecular dynamic simulation approaches have been utilized to retrieve the FDA approved drugs against AD. The predicted MADD protein structure was designed by homology modeling and characterized through different computational resources. Donepezil and galantamine were implanted as standard drugs and drugs were screened out based on structural similarities. Furthermore, these drugs were evaluated and based on binding energy (Kcal/mol) profiles against MADD through PyRx tool. Moreover, pharmacogenomics analysis showed good possible associations with AD mediated genes and confirmed through detail literature survey. The best 6 drug (darifenacin, astemizole, tubocurarine, elacridar, sertindole and tariquidar) further docked and analyzed their interaction behavior through hydrogen binding. Finally, MD simulation study were carried out on these drugs and evaluated their stability behavior by generating root mean square deviation and fluctuations (RMSD/F), radius of gyration (Rg) and soluble accessible surface area (SASA) graphs. Taken together, darifenacin, astemizole, tubocurarine, elacridar, sertindole and tariquidar displayed good lead like profile as compared with standard and can be used as possible therapeutic agent in the treatment of AD after in-vitro and in-vivo assessment.

Alzheimer's disease (AD), a neurodegenerative disorder usually characterized by memory loss in older persons^{1,2}. Globally, it has been observed that around 35 million people are affected by AD annually and this number is believed to double in next 20 years. In USA, 6.7 million American are living with dementia having age greater than 65³. The etiology of AD is highly complex, however, there are some biomarkers including low levels of acetylcholine, β -amyloid ($A\beta$) deposits, tau-protein aggregation, neurofibrillary tangles (NFTs), oxidative stress, and dys-homeostasis of bio-metals are used for the diagnosis of AD^{2,4}. These available clinical therapeutics show only partial effectiveness in ameliorating the AD symptoms⁵.

Drug development is time consuming and overpriced process however, computational techniques particularly drug repurposing is being used in the present time^{6,7}. Drug repositioning is basic computational approach to predict the therapeutic potential of known drugs against different disease by targeting different receptors^{8,9}. However, in present time, medical research emphasizes on the factors that are thought to contribute to AD development,

¹The Steve and Cindy Rasmussen Institute for Genomic Medicine, Nationwide Children's Hospital, Columbus, OH 43205, USA. ²Department of Pharmacology, College of Medicine, Kangwon National University, Chuncheon, South Korea. ³Department of Pediatrics, The Ohio State University, Columbus, OH 43205, USA. ✉email: Mubasher.Hassan@nationwidechildrens.org; Andrzej.Kloczkowski@nationwidechildrens.org

such as tau proteins and A β deposits¹⁰. MAP kinase-activating death domain (MADD) protein is bulky a protein comprises 1647 amino acids and four different domains such as uDENN, cDENN, dDENN and death domain, respectively. Furthermore, six disordered regions are also present in MADD structure with different residues lengths. MADD protein plays a significant role in regulating cell proliferation, survival, and death through alternative mRNA splicing indifferent disease such as Deeah and AD¹¹. MADD protein also links TNF receptor superfamily member 1A (TNFRSF1A) with MAP kinase activation and important for regulatory role in physiological cell death¹².

In the present study, Food and Drug Administration (FDA)-approved drugs were screened against AD by taking double standards donepezil and galantamine through shape-based screening technique. The screened hits underwent molecular docking analysis using PyRx against MADD protein. Moreover, pharmacogenomics analysis was carried out and best drug interacting with AD-medicated genes were shortlisted from the pool of selected drugs. The best-selected drugs were further examined by a docking procedure with AutoDock to check their binding affinities against the MADD protein. Finally, the best-generated docked complexes were further analyzed through molecular dynamics simulations to observe the structural stability through RMSD, RMSF, Rg, and SASA graphs.

Computational methodology

Retrieval of MADD protein sequence

The amino acid sequence of MADD protein having accession number Q8WXG6 (<https://www.uniprot.org/uniprot/Q8WXG6>) was accessed from the UniProt database¹³. MADD protein contains four major domains (uDENN, cDENN, dDENN and Death domain) and unstructured regions..

Modelling of MADD protein and domain assembly

The complete three-dimensional (3D) structure of MADD is not available in Protein Data Bank¹⁴ (PDB; <https://www.rcsb.org/>); therefore, homology modelling based method was used to predict the complete structure of MADD protein. There are different online protein prediction servers, however, trRosetta (transform-restrained Rosetta) is the most recent protein structure prediction server. trRosetta is a web-based platform for fast and accurate protein structure prediction, powered by deep learning and Rosetta (<https://yanglab.nankai.edu.cn/trRosetta/>). However, to predict the complete MADD protein at once using server, its much difficult therefore, all four domains (uDENN, cDENN, dDENN and Death domain) and unstructured/disordered regions were modelled separately using trRosetta. After modelling of all four domains and unstructured/disordered regions, The Domain Enhanced Modeling (DEMO; <https://zhanggroup.org/DEMO/>) was used to assemble all structure using default parameters¹⁵. Demo is a method for automated assembly of full-length structural models of multi-domain proteins. Starting from individual domain structures, DEMO first identify quaternary structure templates that have similar component domains by domain-level structural alignments using TM-align. Replica-exchange Monte Carlo simulations are used to assemble full-length models, as guided by the inter-domain distance profiles collected from the top-ranked quaternary templates. The final models with the lowest energy are selected from Monte Carlo trajectories, followed by atomic-level refinements using fragment-guided MD simulations¹⁵.

Structure analysis of MADD protein

The assemble model structure of MADD protein was analyzed using different computational approaches to check its stability behavior. To do this, initially Ramachandran Plot Server (<https://zlab.umassmed.edu/bu/rama/index.pl>) and MolProbity server (<http://molprobity.biochem.duke.edu/>) were used to check the amino acids and overall protein conformation with respect to phi (ϕ) and psi (ψ) angles by generating Ramachandran graph. The stability behavior of target protein is dependent upon the occurrence of residues in allowed and disallowed regions. Furthermore, the ProtParam tool was employed to predict their theoretical PIs, extinction coefficients, aliphatic and instability indexes, and GRAVY values¹⁶. The overall protein architecture and the statistical percentage values of α -helices, β -sheets, coils, and turns were retrieved from the online VADAR 1.8 server¹⁷. FRST serves to validate the energy of a protein structure¹⁸. The server computes both an overall and a per-residue energy profile of a protein structure. Furthermore, Quality Model Energy Analysis (QMEAN) was employed to further evaluate the model quality (<https://swissmodel.expasy.org/qmean/>). Another known model server SaliLab Model Evaluation Server (<https://modbase.compbio.ucsf.edu/evaluation/>) was employed to check the predicted model quality based on TSVMod and Modeller values. Finally, the modelled structure was further refine using GalaxyWEB (<https://galaxy.seoklab.org/>) before going to utilize it for virtual screening, molecular docking, and dynamic simulation analysis. The graphical representation of model structure was done using Discovery Studio 2.1 Client¹⁹, and UCSF Chimera X²⁰. Furthermore, after prediction of protein model Split-Statistical Potentials Server (<http://aleph.upf.edu/spserver/>) was employed to identify the native conformation behavior and to evaluate the accuracy of protein folds²¹.

Shape-based virtual screening of chemical scaffolds

The Swiss Similarity, an online platform that allows you to identify the similar chemical hits from Food and Drug Administration (FDA) and other libraries with respect to the reference template structure²². In our current research approach, couple of standard drugs; donepezil and galantamine are being used against AD^{5,23,24} were implanted and retrieved similar drugs hits based on structural similarity. The chemical structures of donepezil and galantamine were retrieved from Drug Bank (<https://go.drugbank.com/>) having accession numbers (DB00843 & DB00674) and used as template molecule to screen FDA-approved drugs. All the screened drugs were ranked according to their predicted similarity scoring values. The best screened drugs were sketched in ACD/ChemSketch and utilized for molecular docking experiments.

Prediction of active binding sites of MADD protein

The Prankweb (<http://prankweb.cz/>), an online source that explores the probability of amino acids involved in the formation of active binding sites. Prankweb is a template-free machine learning method based on the prediction of local chemical neighborhood ligandability centered on points placed on a solvent-accessible protein surface²⁵. Points with a high ligandability score are then clustered to form the resulting ligand binding sites. The binding pocket information was not available in PDB; therefore, active binding sites residues of MADD protein were predicted by using Prankweb. The death domain is highly significant domain with functional association with AD¹². Therefore, 3D modeled structure of death domain was utilized and predicts possible binding pockets with high probability values of amino acids²⁵.

Virtual screening using PyRx

Before conducting our docking experiments, all the screened drugs were sketched in ACD/ChemSketch tool and accessed in mol format. Furthermore, UCSF Chimera 1.10.1 tool was employed for energy minimization of each ligand having default parameters such as steepest descent and conjugate gradient steps 100 with step size 0.02 (Å), and update interval was fixed at 10. In PyRx docking experiment, all screened drugs were docked with death domain of MADD using default procedure²⁶. Before, docking binding pocket of target protein was confirmed from Prankweb and literature data. In docking experiments, the grid box dimension values were adjusted as center_X = -0.8961, Y = -1.6716 and Z = 0.3732 whereas, size_X = 37.8273, Y = 36.5416 Z = 36.5756, respectively, with by default exhaustiveness = 8 value. The grid box size was adjusted on binding pocket residues to allow the ligand to move freely in the search space. Furthermore, the generated docked complexes were keenly analyzed to view their binding conformational poses at active binding site of MADD protein. Moreover, these docked complexes were evaluated based on the lowest binding energy (Kcal/mol) values and binding interaction pattern between ligands and target protein. The graphical depictions of all the docked complexes were accomplished by UCSF Chimera 1.10.1 and Discovery Studio (2.1.0), respectively.

Furthermore, another docking experiment was employed on best screened drugs against MADD protein using AutoDock 4.2 tool²⁷. In brief, for receptor protein, the polar hydrogen atoms and Kollman charges were assigned. For ligand, Gasteiger partial charges were designated, and non-polar hydrogen atoms were merged. All the torsion angles for screened drugs were set free to rotate through the docking experiment. A grid map of 80 × 80 × 80 Å was adjusted on the binding pocket of MADD to generate the grid map and to get the best conformational state of docking. A total of 100 number of runs were adjusted using docking experiments. The Lamarckian genetic algorithm (LGA) and empirical free energy function were applied by taking docking parameters default²⁸. All the docked complexes were further evaluated on lowest binding energy (kcal/mol) values and hydrogen and hydrophobic interactions analysis using Discovery Studio (2.1.0) and UCSF Chimera 1.10.1.

Designing of pharmacogenomics networks

To design the pharmacogenomics network model for best-selected drugs, Drug Gene Interaction Databases (DGIdb) (<https://www.dgidb.org/>) and Drug Signatures Database (DSigDB) (<http://dsigdb.tanlab.org/DSigDBv1.0/>) were employed to obtain the possible list of different disease-associated genes. Furthermore, a detailed literature survey was performed against all predicted genes to identify its involvement in AD. Moreover, clumps of different diseases associated genes were sorted based on MADD and remaining disease-associated genes were eliminated from the dataset.

Molecular dynamics (MD) simulations

The best screened drugs-complexes having good energy values were selected to understand the residual backbone flexibility of protein structure; MD simulations were carried out by Groningen Machine for Chemicals Simulations (GROMACS 4.5.4 package²⁹, with GROMOS 96 force field³⁰). The protein topology was designed by pdb2gmx command by employing GROMOS 96 force field. Moreover, simulation box with a minimum distance to any wall of 10 Å (1.0 nm) was generated on complex by editconf command. Moreover, box was filled with solvent molecules using gmh solvate command by employing spc216.gro water model. The overall system charge was neutralized by adding ions. The steepest descent approach (1000 ps) for protein structure was applied for energy minimization. For energy minimization the nsteps = 50,000 were adjusted with energy step size (emstep) 0.01 value. Particle Mesh Ewald (PME) method was employed for energy calculation and for electrostatic and van der Waals interactions; cut-off distance for the short-range VdW (rvdw) was set to 14 Å, whereas neighbor list (rlist) and nstlist values were adjusted as 1.0 and 10, respectively, in em.mdp file³¹. This method permits the use of the Ewald summation at a computational cost comparable with that of a simple truncation method of 10 Å or less, and the linear constraint solver (LINCS)³² algorithm was used for covalent bond constraints and the time step was set to 0.002 ps. Finally, the molecular dynamics simulation was carried out at 100 ns with nsteps 50,000,000 in md.mdp file. Different structural evaluations such as root mean square deviations and fluctuations (RMSD/RMSF), solvent accessible surface areas (SASA) and radii of gyration (Rg) of backbone residues were analyzed through Xmgrace software (<http://plasma-gate.weizmann.ac.il/Grace/>).

Results and discussion

The overall computational drug repositioning flowchart showed the multiple steps involved in this study (Fig. 1). A total of 631 drugs have been evaluated by employing different computational resources through PyRx screening, pharmacogenomics analysis, molecular docking, and MD simulations, respectively.

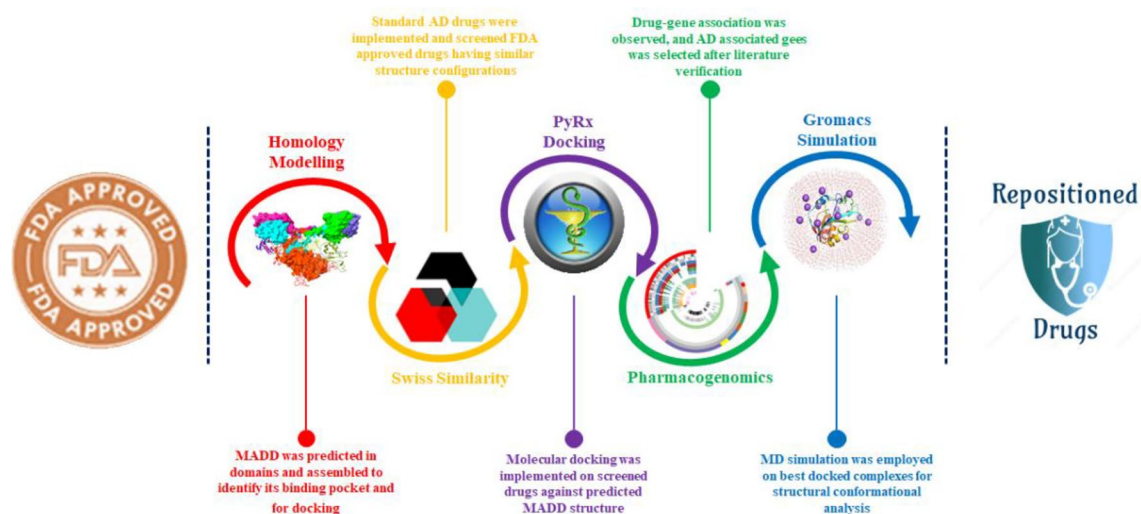


Figure 1. Proposed mechanistic flowchart of repositioned drugs.

ProtParam analysis of MADD protein

ProtParam (<https://web.expasy.org/protparam/>) is an online tool which analyse the protein based on various physical and chemical parameters, respectively. The significant parameters include molecular weight (mg/mol), theoretical *pI*, amino acid composition, atomic composition, extinction coefficient, estimated half-life, instability/aliphatic indexes, and grand average of hydropathicity (GRAVY), respectively. The generated theoretical *pI* value of MADD protein is calculated by the accumulation of average isotopic masses and *pK* values of linear amino acids present in the proteins. The prior published research data depicted that proteins are distributed across a wide range of *pI* values (4.31–11.78)³³. The MADD protein exhibited 5.49 *pI* value which is comparable with the standard values (4.31–11.78). Moreover, the aliphatic index value also showed the stability and relative volume occupied by aliphatic side chain residues. The predicted physicochemical properties showed the reliability, efficacy, and stability of the MADD protein. The predicted values of both instability and aliphatic indexes 58.81 and 74.96 are justifiable with standard values. The GRAVY value is the sum of hydropathy values of all residues in protein³⁴. The prior research reports justified that the GRAVY negative and positive values show the hydrophilic and hydrophobic behavior of protein structure³³. The negative GRAVY value (– 0.517) of MADD protein indicates the hydrophilic behavior (Table 1).

Structural assessment of MADD protein

MAP kinase-activating death domain (MADD) is a human protein encoded by *MADD* gene³⁵. MADD, a bulky protein structure which comprises 1647 amino acids having molecular mass 183.303 KDa. The structural analysis showed that MADD contains four major domains such as uDENN (14–268 AA), cDENN (289–429 AA), dDENN (431–565 AA) and death domain (1340–1415 AA), respectively with disordered regions (<https://www.uniprot.org/uniprot/Q8WVG6>) (Fig. 2).

VADAR analysis

VADAR is an online server which predict the protein volume, area, dihedral angle reports and statistical evaluation. The generated MADD model structure showed different architectures related to α -helices, β -sheets, coils and turn, respectively. The overall protein structure analysis showed that MADD consists of 25% α -helices, 19% β -sheets, 55% coils and 20% turns, respectively. Moreover, Ramachandran plots and values depicted that 92.68%

Protein parameters	Predicted values
Number of amino acids	1165
Theoretical <i>PI</i>	5.49
Negatively charged residues (Asp + Glu)	157
Positively charged residues (Arg + Lys)	131
Total number of atoms	17,974
Instability index	58.81
Aliphatic index	74.96
GRAVY	– 0.517

Table 1. The physicochemical properties of MADD protein.

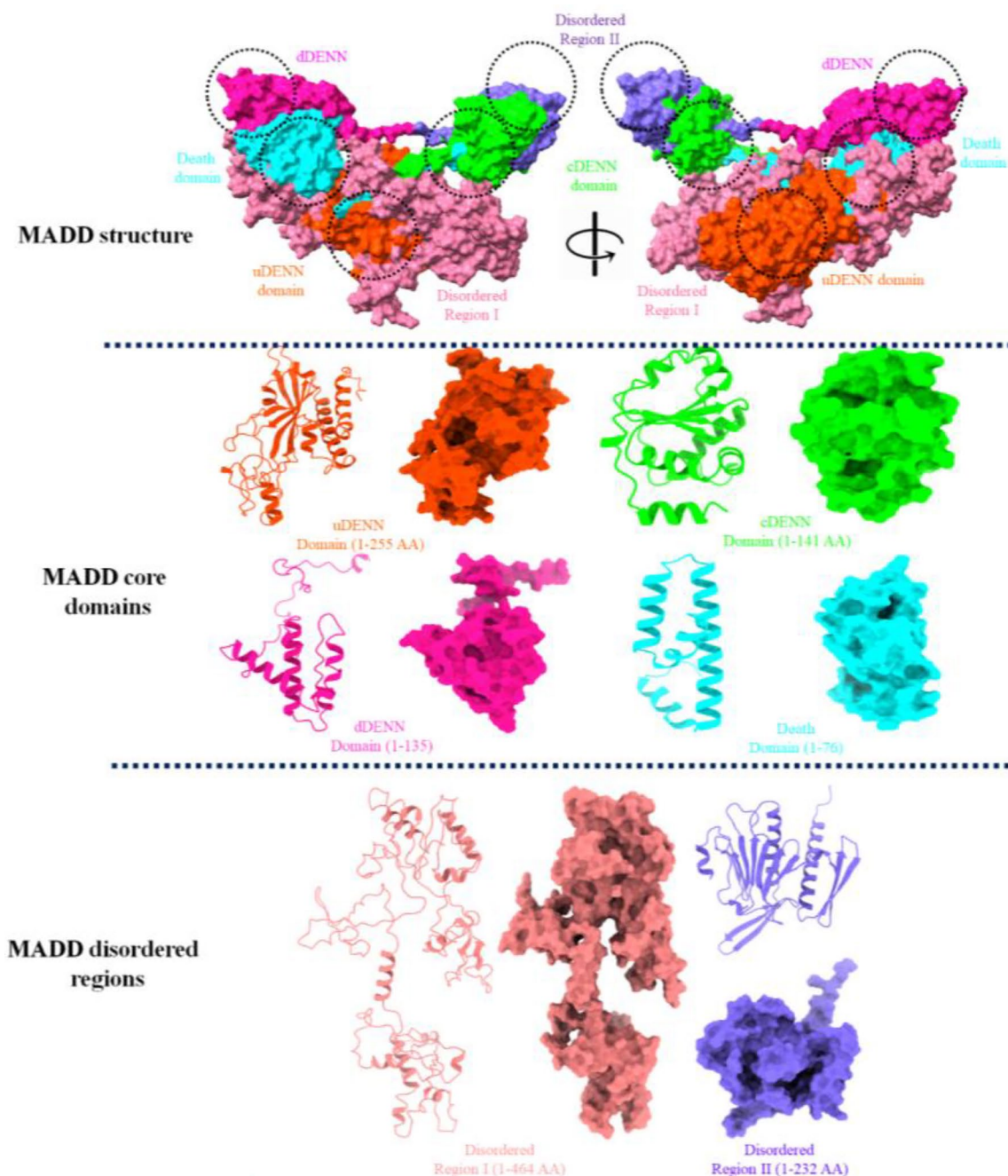


Figure 2. The overall protein structure of MADD protein. The figure showed the three main parts, the overall protein structure, its four core domains and couple of disordered regions.

of amino acids were present in favored region with good accuracy of phi (ϕ) and psi (ψ) angles which showed the good accuracy of our predicted model.

Galaxy refine analysis

Galaxy-refine is an good source to resolve the ambiguities in the modelled structure based on different parameters such as GDT-HA, RMSD, MolProbity, clash score, poor rotamers and Rama favored, respectively³⁶. The initial predicted structure of MADD protein depicted MolProbity: 3.809–2.871, clash score: 88.4–47.8, poor rotamers: 5.7–1.4 and Rama favored: 72.4–85.8, respectively whereas, the values have been rectified to improve the modelled MADD structure (Supplementary Table S1). Moreover, the online Ramachandran graph server (<https://www.umassmed.edu/zlab/>) generate both Ramachandran graphs which have been mentioned in Fig. 3. The comparative results showed that the Galaxy refine clearly improved the modelled MADD structure which can be further implied for structure and docking analysis.

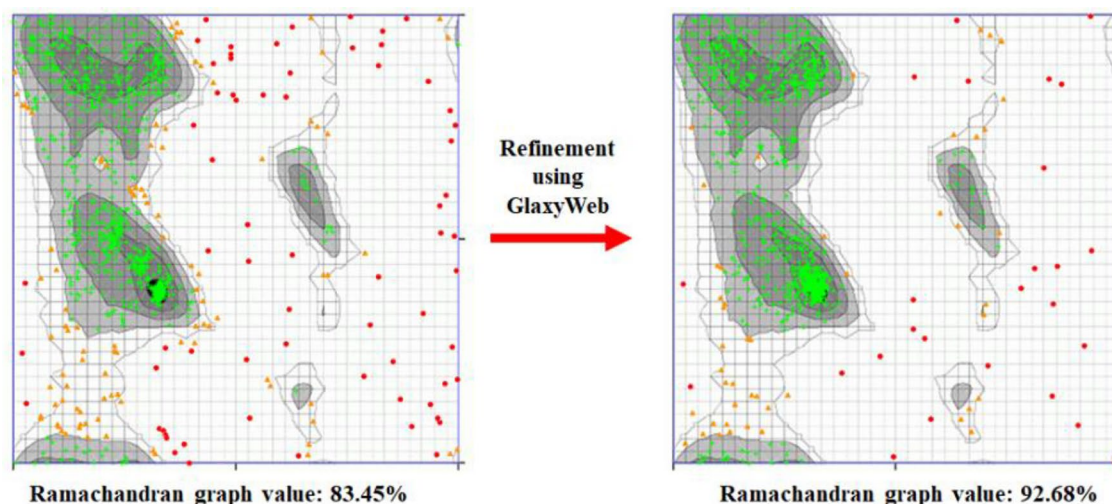


Figure 3. Ramachandran graphs of predicted MADD protein.

FRST energy validation against MADD

The energy validation of predicted MADD structure was analyzed using FRST evaluation tool based on overall and a per-residue energy profile of a protein structure. The FRST energy calculation is composed of rapdf pairwise potential, solvation potential, backbone hydrogen bonds and torsion angle potential and composite score values (<http://protein.cribi.unipd.it/frst/>). The rapdf potential³⁷ is a distance-dependent residue-specific all-atom probability discriminatory function. Similarly, solvation potential to likelihood for each of 20 amino acids to adopt a given relative solvent accessibility is used to derive the pseudo-energy³⁸. The torsion angle potential (TORS) is derived from the propensities of each amino acid to adopt different combinations of (ϕ , ψ) torsion angles³⁹. The total energy is again summed over all individual contributions in a protein. In our generated MADD results, rapdf, solvation, torsion and composite FRST energies (Kcal/mol) which showed the stability of model structure (Table 2).

Quality model energy analysis

Qualitative Model Energy ANalysis (QMEAN) is a composite scoring function which derive both global and local absolute quality estimates based on one single model (<https://swissmodel.expasy.org/qmean/>). The generated results showed that MADD protein exhibited -6.64 value which is comparable with standard values (0,1). The prior data showed that different residues clumps showed lowest score value 0.1 which represents the quality assessment of predicted MADD model. However, most amino acids patches in the predicted model showed higher values >0.6 depicts accurate and stable behavior of MADD protein. The blue peak showed highest prediction value having best quality results (>0.8) of predicted model. Moreover, the purple color represents also showed good accuracy of MADD protein with scoring values range from 0.6 to 0.8. However, the orange values showed the de-stable behavior of MADD protein with values less than 0.6. The overall results showed that predicted MADD model exhibited good stable behavior and could be used for further analysis (Fig. 4).

Native conformational behavior evaluation

After prediction the protein models, native conformation behavior is significant parameter is to evaluate the accuracy of protein folds. SPS server (<http://aleph.upf.edu/spserver/index.php/init.html>), is a knowledge-based scoring functions used for correct folding of proteins, stability of mutant proteins, and assess outcomes of docking experiments. The generated results were evaluated based on five different parameters such as PAIR, ES3DC, ECOMB, ELOCAL, and E3DC respectively. The PAIR and ES3DC parameters are focused on amino acid frequencies along distances and their environments such as hydrophobicity of each amino acid, solvent accessibility, and secondary structure, respectively. Figure 5A, B showed that residues fluctuations with respect to z-score values. In PAIR parameters analysis, residues showed stable frequency throughout the protein structure except amino

Protein energy parameters	Predicted scores (Kcal/mol)
Rapdf energy	$-19,038.2$
Solvation energy	9.04
Torsion energy	-50.96
Composite FRST energy	$-60,911.62$

Table 2. The energy evaluation of MADD protein.

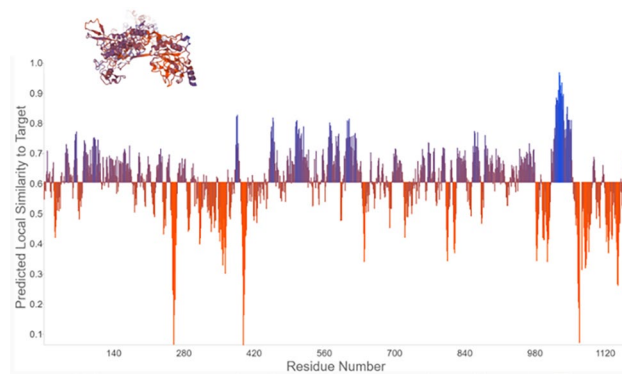


Figure 4. QMEAN Quality assessment of MADD protein.

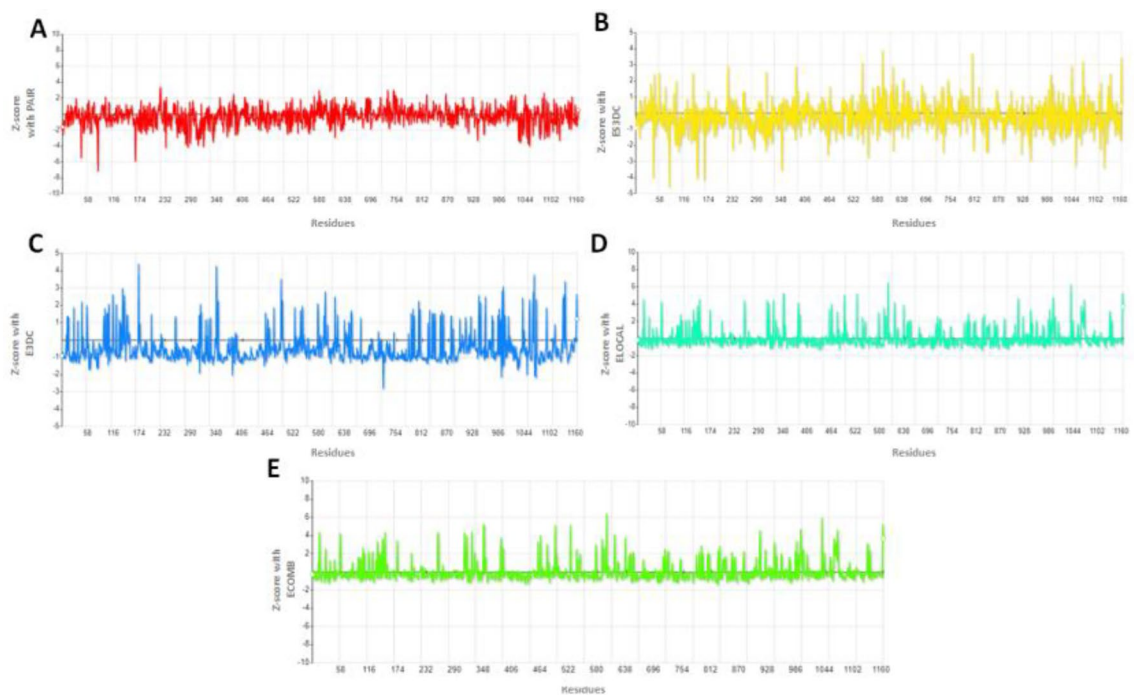


Figure 5. (A–E) SPS analysis of MADD protein to predict their folding and native conformation pattern.

acids at positions 58, 60, 174, 696 and 1100, respectively. The graph line remains stable at center value 0 with little deviations range from 2 and -2 . In ES3DC analysis in correlation with Z-score, the generated graph line (yellow) showed high fluctuations at the terminal part of MADD protein. However, the average value ranges from 3 to -3 in the energy folding graph. Our results depicted that MADD protein exhibited hydrophobicity and solvent accessibility properties, respectively. Moreover, both E3DC and ELOCAL parameters are also implicated on MADD protein based on amino acid frequencies along distances of pairs referred by the hydrophobicity of the amino acids and the rest of their environments, whereas ECOMB is combinatorial scores of all three parameters such as ES3DC, ELOCAL and E3DC, respectively. Figure 5C displayed the residual fluctuations graph at different positions in the MADD structure whereas, ELOCAL parameter showed less fluctuations based on Z-score values (Fig. 5D). In combine effects, the ECOMB parameter exhibited stable behavior and good folding of model MADD protein. The fluctuation peaks were range from 0 to 3, however, at various position range raised up to 4 (Fig. 5E).

Binding pocket analysis of MADD protein

Generally, binding pocket is the core position of ligands in the active region of protein⁴⁰. Prankweb is a novel machine learning method for prediction position of ligand binding sites inside the protein structure⁴¹. The predicted results showed five different binding pockets with different scoring values 15.4, 4.42, 3.68, 2.44 and 1.41, respectively. The pocket-1 exhibited high score value 15.4 as compared to other binding pockets and constitutes Met-1004, Ile-1005, Arg-1007, Tyr-1008, Leu-1009, Leu-1011, Leu-1019, Glu-1020, Glu-1023, Leu-1026, Leu-1027, Leu-1030, Leu-1055, Lys-1058, Ser-1059, His-1060, and Ile-1061 amino acids. Soluble Accessible Surface (SAS) area represents the area having propensity to interact with neighboring atoms. The pocket 1 showed good SAS

value 152 as compared to other binding pockets values (66, 49, 28 and 18, respectively) with different amino acids of death domain of MADD protein. Moreover, the probability value of pocket 1 was also better as compared to other probabilities values (Fig. 6A, B).

Shape based screening and retrieval of similar FDA approved drugs

In drug-repositioning approach, shape-based screening, pharmacogenomics and molecular docking simulation are significant parameters to predict the possible drugs from FDA approved medications by considering protein targets^{5,42}. Donepezil and galantamine were used as standard drug against AD and used as template to screen FDA approved drug having similar skeleton similarity. In our computational results, Swiss-Similarity results showed 282 drugs were retrieved with donepezil and 351 against galantamine. The scoring values FDA approved drugs based on structural similarity scoring values range from 1.000 to 0.010 and 1.000 to 0.134 for donepezil and galantamine, respectively (Supplementary Tables S2 and S3). The screened drugs were ranked based on similarity scoring values, ranged for 0–1. The 0 value represents dissimilarity between compounds whereas, 1 is used for highly identical compounds in screening approach⁵. In our computational results, drugs depicted good similarity scoring values range from 1 to 0.111. In donepezil screening results, DB07701 and DB3393 were exhibited scoring values 0.999 and 0.837, respectively. Furthermore, in galantamine screening results, it has been observed that DB00318 (0.979), DB01466 (0.977), and DB11490 (0.974) showed scoring values and DB14703 depicted lowest structure similarity result 0.134. The top 100 screened drugs from each standard (donepezil and galantamine) were selected for molecular docking analysis to predict the most suitable candidate having good binding affinity values against MADD protein.

Virtual screening using PyRx

PyRx is a virtual screening software for computational drug discovery that can be used to screen libraries of compounds against potential drug targets. In PyRx, donepezil-MADD docking results, among 100 screened drugs (Table S4), 72 drugs showed higher docking energy values as compared to standard donepezil (Table 3). Similarly, In PyRx, galantamine-MADD docking results, among 100 screened drugs (Table S5), 67 drugs showed higher docking energy values as compared to standard galantamine (Table 4).

Pharmacogenomics analysis

Based on swiss similarity and virtual screening result, the selected drugs further undergo for pharmacogenomics analysis to check their possible interaction with genes encoded proteins and their association with AD. Multiple reports also justify this approach as worthwhile to predict the possible drug having repositioned functionality^{5,12}. All the screened drug from both standard (donepezil and galantamine) exhibited good interaction scoring values with predicted genes which showed good correlation with AD. From donepezil screening, our results showed that 10 from 35 drugs exhibited good interaction scoring values and association with AD. The darifenacin showed good interaction scoring values with CHRM3 (0.85), CHRM2 (0.38), CHRM1 (0.29) and CYP2D6 (0.04) which have correlation with AD. The other drug astemizole showed interaction with multiple genes (14) which have association with multiple diseases. The 9 genes such as CYP2J2, HPSE, ABCB1, PPARC, CYP2D6, IDH1, CYP3A4, AR, and TP53 were directly associated with AD. The predicted results showed that astemizole showed highest interaction score 0.90 as compared to other genes. In tubocurarine gene network, 5 genes were interacted and among these four 2 (CHRNA2 and KCNN2) genes were showed interaction with AD. Both CHRNA2 and KCNN2 genes exhibited good interaction scoring values 6.37 and 4.24, respectively. Another important screened

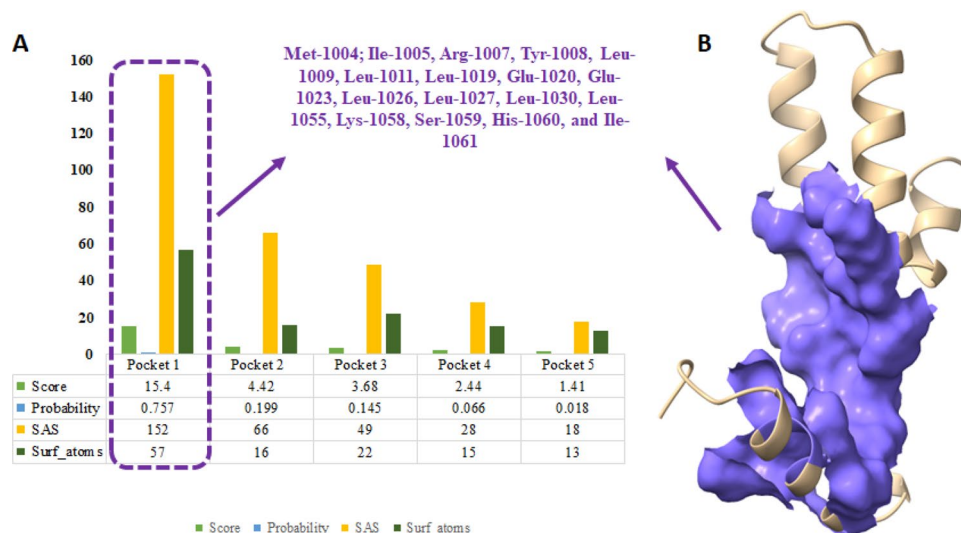


Figure 6. (A) Predicted binding pockets represented by graphs lines and scoring values of death domain of MADD protein. (B) the predicted model of death domain and core part has been depicted in purple color in surface format.

Drugbank IDs	Drugs	Binding affinity (Kcal/mol)	Drugbank IDs	Drugs	Binding affinity (Kcal/mol)
DB00496	Darifenacin	- 8.1	DB08927	Amperozide	- 7.7
DB00637	Astemizole	- 8.4	DB08950	Indoramin	- 8.6
DB01199	Tubocurarine	- 8.5	DB09063	Ceritinib	- 8
DB01238	Aripiprazole	- 7.9	DB09083	Ivabradine	- 7.5
DB02929	K201 free base	- 7.7	DB11376	Azaperone	- 7.7
DB04835	Maraviroc	- 7.7	DB11732	Lasmiditan	- 8.8
DB04842	Fluspirilene	- 8.5	DB11793	Niraparib	- 8.1
DB04872	Osanetant	- 9.2	DB12082	Vesnarinone	- 8.2
DB04881	Elacridar	- 10.2	DB12096	PF-05175157	- 8.3
DB05171	E-2012	- 7.9	DB12289	DB12289	- 8.6
DB05414	Pipendoxifene	- 8.4	DB12341	LY-2456302	- 8.3
DB05422	OPC-14523	- 7.5	DB12408	PF-03635659	- 8.4
DB05713	LY-517717	- 9.1	DB12731	Daporinad	- 7.8
DB06144	Sertindole	- 8.1	DB12837	UK-500001	- 9.2
DB06240	Tariquidar	- 10.4	DB12867	Benperidol	- 8.3
DB06306	Onalespib	- 7.9	DB12886	GSK-1521498	- 10.3
DB06401	Bazedoxifene	- 8.4	DB12981	XL-888	- 8.1
DB06446	Dotarizine	- 8.1	DB13080	Roluperidone	- 8
DB06454	Sarizotan	- 9.2	DB13276	Idanpramine	- 8.8
DB06555	Siramesine	- 9.3	DB13310	Ormeloxifene	- 7.8
DB16182	CXD101	- 8.9	DB13393	Emetine	- 7.8
DB15398	Dihydrocapsiate	- 5.7	DB13403	Oxypertine	- 7.9
DB15688	Vazegepant	- 11.1	DB13511	Clebopride	- 7.4
DB14641	Estriol tripropionate	- 7.3	DB13687	Niaprazine	- 7.4
DB08810	Cinitapride	- 7.6	DB13766	Lidoflazine	- 8.8
DB15120	GSK-239512	- 8.3	DB13790	Fipexide	- 7.5
DB15377	ATB-346	- 7.7	DB13865	Dehydroemetine	- 7.6
DB16080	Acolbifene	- 9	DB13954	Estradiol cypionate	- 8
DB16124	Chiauranib	- 9.2	DB00843	Donepezil	- 7.4

Table 3. Screening of FDA approved drugs using donepezil. Significant values are in [bold].

drug which exhibited good interaction prediction with AD is aripiprazole through interaction with different genes. The drug-gene association analysis showed that out of 14 genes, eleven (DRD2, HTR1A, ANKK1, SH2B1, HTR2A, CNR1, FAAH, HTR1B, HTR2C, ABCB1, CYP2D6) possessed good interaction scoring values and are directly involves in AD.

Fluspirilene-gene interactions analysis also showed their intimation with AD by targeting multiple genes. The predicted results showed that six gene such as DRD2, HTR1E, XBP1, HTR2A, HTR1A, and PPARD were showed their association with AD with different interaction scoring values. In elacridar-genetic complex, two genes ABCG2 (1.54) and ABCB1 (0.27) were observed having showed their interaction with AD. Another important screened drug was sertindole which showed interactions multiple genes involves in AD and other diseases. A total of 17 genes were observed showed interaction with sertindole and from 17, eight genes (DRD2 (0.15), HTR2A (0.14), HTR2C (0.17), HTR1E (0.1), HTR1A (0.03), HTR1B (0.05), CYP2D6 (0.01), CYP3A4 (0.01)) showed association with AD with different interaction scoring values. Tariquidar interacted with ABCB1 and ABCG2 with scoring values 0.66 and 1.03, respectively. Sarizotan is another screened drug shows interactions with HTR1A (0.91) and DRD2 (0.36) having good interaction score values with AD. Similarly, fipexide interacted with CYP2D6 (0.03) and CYP3A4 (0.02) also depicted good correlation with AD (Table 5).

In galantamine pharmacogenomics results, forty screened drugs having good similarity score has been predicted having possible correlation with AD mediated genes. However, from forty, eight screened drugs have been elected having good interaction scoring values as well as exhibited good association with AD mediated genes. Morphine shows interactions with 24 genes having association with different diseases and only seven genes possessed association with AD. These seven genes PDYN (4.11), OPRK1 (0.23), PER1 (2.05), HMOX2 (2.05), ABCB1 (0.09), CYP2D6 (0.01), DRD2 (0.02) may predict the good therapeutic behavior of morphine as an anti-AD drug. Codeine is another screened drug extracted through galantamine that could be use as repositioned drug against AD. Our drug-gene predicted results showed that eight genes OPRD1 (1.22), OPRM1 (0.58), OPRK1 (0.63), UGT2B7 (0.76), ABCB1 (0.13), CYP3A4 (0.02), CYP2D6 (0.01), and AR (0.01) were interacted having different interaction values. The literature mining showed that four genes among eight were involved in AD. Quinine-gene interaction analysis showed that CYP3A7 (1.27), SLC29A4 (0.64), COP1 (1.27), IL2 (0.6), G6PD (0.18), ABCB1 (0.03), CYP3A4 (0.01), and CYP2D6 (0.01). Moreover, from gene literature mining it has been observed that

Drugbank IDs	Drugs	Binding affinity (Kcal/mol)	Drugbank IDs	Drugs	Binding affinity (Kcal/mol)
DB00295	Morphine	- 7.1	DB06444	Dexanabinol	- 6.8
DB00318	Codeine	- 7.4	DB06578	Tonabersat	- 7.5
DB00424	Hyoscyamine	- 7.1	DB07905	Hypothemycin	- 7.6
DB00468	Quinine	- 7.2	DB09039	Eliglustat	- 7
DB00497	Oxycodone	- 7.5	DB09184	Edivoxetine	- 6.7
DB00521	Carteolol	- 6.7	DB09196	Lubazodone	- 6.7
DB00572	Atropine	- 7	DB09209	Pholcodine	- 7.7
DB00611	Butorphanol	- 7.3	DB11181	Homatropine	- 7
DB00654	Latanoprost	- 6.7	DB11411	Fenprostalene	- 6.9
DB00688	Mycophenolate mofetil	- 7.2	DB11490	Nalorphine	- 6.8
DB00704	Naltrexone	- 7.6	DB11711	Navarixin	- 7.7
DB00844	Nalbuphine	- 7.6	DB12057	ORM-12741	- 7.3
DB00905	Bimatoprost	- 7.5	DB12179	Secoisolaricresinol	- 6.6
DB00908	Quinidine	- 6.9	DB12464	Bevenopran	- 7.5
DB00921	Buprenorphine	- 6.8	DB12543	Samidorphan	- 6.8
DB00973	Ezetimibe	- 7.8	DB12637	Onapristone	- 7.5
DB01183	Naloxone	- 7.2	DB12884	Lavoltidine	- 7.4
DB01192	Oxymorphone	- 7.3	DB13471	Nalfurafine	- 8
DB01229	Paclitaxel	- 7.6	DB13718	Hydroquinine	- 7.3
DB01346	Quinidine barbiturate	- 7.2	DB14035	Englitazone	- 8
DB01450	Dihydroetorphine	- 7.4	DB14881	Oliceridine	- 7
DB01466	Ethylmorphine	- 7.1	DB15241	Methylsamidorphan	- 7.3
DB01469	Acetorphine	- 7.2	DB15300	Hydroquinidine	- 7.2
DB01477	Codeine methylbromide	- 7	DB15439	Navoximod	- 7.2
DB01480	Cyprenorphine	- 7	DB15495	Rocaglamide	- 7.2
DB01497	Etorphine	- 7.5	DB15496	Didesmethylocaglamide	- 7.8
DB01505	Etoxidine	- 5.7	DB16243	TBA-7371	- 7.7
DB01512	Hydromorphenol	- 6.7	DB16287	Penequinine, Penecyclidine	- 7.2
DB01548	Diprenorphine	- 7.2	DB16351	Volinanserine	- 6.6
DB01551	Dihydrocodeine	- 7.5	DB04865	Omacetaxine mepesuccinate	- 7.4
DB01565	Dihydromorphine	- 6.7	DB04861	Nebivolol	- 7.7
DB01573	Benzylmorphine	- 8.3	DB06217	Vernakalant	- 7
DB02205	Rutamarin alcohol	- 7.1	DB06230	Nalmefene	- 7.3
DB04509	N-Methylnaloxonium	- 7.9	DB00674	Galantamine	- 6.7

Table 4. Screening of FDA approved drugs using galantamine against MADD. Significant values are in [bold].

5 genes were involved in AD. Similarly, atropine, nalbuphine, quinidine, volinanserine and vernakalant are also screened drugs interacting with different genes which are linked with AD (Table 6).

Molecular docking using autodock

Docking energy analysis against death domain of MADD

The selected drugs-death domain docked complexes were analyzed based on lowest binding energy values (Kcal/mol) and hydrogen/hydrophobic interaction analyses. Results showed that all drugs showed good binding energy values (Kcal/mol) and binds within the active site with appropriate conformational poses (Table 7). Docking energy values is most significant parameter to screen and evaluate the drugs in binding with target proteins^{5,203-206}. Among all, six drugs including darifenacin (- 7.59 kcal/mol), astemizole (- 7.19), tubocurarine (- 8.26), elacridar (- 7.72), sertindole (- 7.58) and tariquidar (- 8.42) showed higher than - 7 (kcal/mol) docking energy values. The ligand efficiency is a useful metric for lead selection using computational resources²⁰⁷. Ligand efficiency is a way of normalizing the potency and MW of a compound to provide a useful comparison between compounds with a range of MWs and activities. In our docking results, the predicted ligand efficiency (LE) results, showed that all drugs exhibited good LE values, whereas lowest value is considered as most significant compared to other. The comparative results showed that Tubocurarine, Elacridar and Tariquidar exhibited - 0.18 value which was lowest compared to rest of all drugs.

Another significant parameter in drug analysis is inhibition constant (Ki). Autodock uses the binding energy (Kcal/mol) to calculate the inhibition constant. The binding energy is the free energy change for the protein-inhibitor interaction (ΔG). This is used to determine the inhibition constant (ki) which is, in turn, the dissociation constant (Kd) of the protein-inhibitor complex. In our predicted results, morphine, codeine, quinine, darifenacin,

Drugs	Genes	Interaction score	Disease associations	Refs.
Darifenacin	CHRM3	0.85	AD	43
	CHRM4	0.54	Schizophrenia	44
	CHRM5	0.5	Schizophrenia	45
	CHRM2	0.38	AD	46
	CHRM1	0.29	AD	47
	CYP2D6	0.04	AD	48
Astemizole	EED	9.09	Cohen-Gibson	49
	HRH1	0.35	Allergic rhinitis	50
	CYP2J2	0.91	AD	51
	KCNH1	0.76	Epilepsy	52
	HPSE	0.7	AD	53
	KCNH2	0.15	Short QT syndrome	54
	ABCB1	0.02	AD	55
	PPARD	0.03	AD	56
	CYP2D6	0.01	AD	57
	IDH1	0.01	AD	58
	GMNN	0.01	Meier-Gorlin syndrome	59
	CYP3A4	0.01	AD	57
	AR	0.01	AD	60
	TP53	0.01	AD	61
Tubocurarine	ZACN	12.73	Neoplasm	62
	CHRNA2	6.37	AD	63
	KCNN2	4.24	AD	64
	KCNN3	3.18	Neoplasm metastais	65
	KCNN1	2.55	Leukemia	66
Aripiprazole	TAAR6	7.96	Bipolar Disorder	67
	DRD2	0.83	AD	68
	HTR1A	0.38	AD	69
	MC4R	1.11	Obesity	70
	ANKK1	0.99	AD	68
	SH2B1	0.88	AD	71
	HTR2A	0.22	AD	72
	HTR1D	0.2	Adenocarcinoma	73
	CNR1	0.41	AD	74
	FAAH	0.38	AD	75
	HTR1B	0.18	AD	76
	HTR2C	0.12	AD	72
	ABCB1	0.03	AD	55
CYP2D6	0.01	AD	57	
Maraviroc	CCR5	27.58	AD	77
Fluspirilene	DRD2	0.13	AD	68
	HTR1E	0.09	AD	72
	XBP1	0.15	AD	78
	HTR1D	0.05	Adenocarcinoma	73
	HTR2A	0.04	AD	72
	HTR1A	0.03	AD	69
	HRH1	0.02	Allergic rhinitis	50
	PPARD	0.02	AD	56
	THPO	0.04	Amegakaryocytosis	79
	NPSR1	0.03	Allergic asthma	80
Osanetant	TACR3	3.86	Hypogonadotropic hypogonadism	81
	TACR2	3.03	AD	82
	TACR1	0.59	Bipolar	83
Elacridar	ABCG2	1.54	AD	84
	ABCB1	0.27	AD	55
LY-517717	F10	5.79	Factor X Deficiency	85
Continued				

Drugs	Genes	Interaction score	Disease associations	Refs.
Sertindole	DRD2	0.15	AD	68
	HTR2A	0.14	AD	72
	HTR2C	0.17	AD	72
	HTR6	0.31	Schizophrenia	86
	KCNH2	0.08	Short QT syndrome	54
	ADRA1D	0.21	Crohn Disease	87
	HTR1E	0.1	AD	72
	HTR1D	0.06	Adenocarcinoma	73
	ADRA1B	0.13	Seizures	88
	HTR1A	0.03	AD	69
	ADRA1A	0.12	Schizophrenia	89
	HTR1F	0.12	Schizophrenia	90
	HTR1B	0.05	AD	76
	HRH1	0.02	Allergic rhinitis	50
	DRD4	0.05	Mental Depression	91
	CYP2D6	0.01	AD	48
CYP3A4	0.01	AD	57	
Tariquidar	ABCB1	0.66	AD	55
	ABCG2	1.03	AD	84
Onalespib	ALK	0.56	Neoplasms	92
	HSP90AA1	0.23	Breast Carcinoma	93
Bazedoxifene	IL6ST	10.61	Rheumatoid Arthritis	94
	IL6R	3.54	Rheumatoid Arthritis	95
	ESR2	0.69	Breast neoplasm	96
	ESR1	0.32	Breast neoplasm	96
Sarizotan	HTR1A	0.91	AD	69
	DRD2	0.36	AD	68
CXD101	HTT	0.32	Huntington Disease	97
Acolbifene	ESR2	0.46	Breast neoplasm	96
	ESR1	0.32	Breast neoplasm	96
Chiauranib	AURKB	0.27	Liver carcinoma	98
	FLT1	0.19	Breast neoplasm	99
	FLT4	0.18	Milroy Disease	100
	KDR	0.12	Hemangioma	101
Amperozide	DRD1	0.19	Bipolar Disorder	102
	CYP3A4	0.04	AD	57
Indoramin	ADRA1A	0.59	Schizophrenia	89
	ADRA1D	0.45	Crohn Disease	87
	ADRA1B	0.27	Seizures	88
Ceritinib	EML4	4.77	Lung Carcinoma	100
	ALK	4.37	Neoplasms	92
	TSSK1B	1.99	Systemic Scleroderma	103
	NPM1	1.52	Leukemia	104
	ROS1	0.73	Adenocarcinoma of lung	105
	IGF1R	0.42	Fetal Growth Retardation	106
	INSR	0.26	Donohue Syndrome	107
	MAP2K1	0.21	Cardio-facio-cutaneous syndrome	108
	SRC	0.18	Thrombocytopenia	109
	CYP3A4	0.01	AD	57
	FLT3	0.06	Leukemia	110
	ABCB1	0.04	AD	55
Ivabradine	HCN3	4.24	Diabetes Mellitus	111
	MALAT1	4.24	Breast neoplasm	112
	HCN1	3.18	Epileptic encephalopathy	113
	HCN4	2.55	Sick Sinus Syndrome	114
	CYP3A4	0.01	AD	57
Continued				

Drugs	Genes	Interaction score	Disease associations	Refs.
Lasmiditan	HTR1F	10.97	Schizophrenia	90
Niraparib	PARP2	6.06	Lipodystrophy	115
	SLFN11	4.71	Malignant Neoplasms	116
	PARP1	3.54	Breast neoplasm	117
	BRCA1/2	1.41	Breast neoplasm	118
	ATR	0.79	Seckel syndrome	119
	ATM	0.13	Ataxia Telangiectasia	120
	PTEN	0.07	Hamartoma Syndrome	121
	IDH1	0.04	AD	58
Vesnarinone	THBS1	2.27	Diabetic Retinopathy	122
	NT5E	1.3	Calcification of Joints	123
	FAS	0.96	Autoimmune Lymphoproliferative Syndrome	124
	PDE3A	0.4	Brachydactyly	125
	CYP3A4	0.02	AD	57
	KCNH2	0.03	Short QT syndrome	54
	TP53	0.05	AD	61
PF-05175157	ACACB	21.22	Obesity	126
LY-2456302	OPRM1	0.17	Alcoholic Intoxication	127
	OPRD1	0.33	Alcoholic Intoxication	127
Daporinad	NAMPT	42.43	Colorectal Carcinoma	128
Benperidol	DRD4	0.33	Mental Depression	91
	CYP2D6	0.04	AD	48
	DRD2	0.12	AD	68
GSK-1521498	OPRM1	0.51	Alcoholic Intoxication	127
XL-888	NRAS	0.66	Colorectal Carcinoma	129
	HSP90AB1	0.42	Pulmonary Fibrosis	130
	BRAF	0.33	Melanoma	94
Emetine	HIF1A	0.19	Hypertensive disease	131
	MTOR	0.1	Focal cortical dysplasia	132
	ATXN2	0.05	Spinocerebellar Ataxia-II	133
	ATAD5	0.04	Carcinoma, Ovarian Epithelial	134
	AR	0.01	Malignant neoplasm of prostate	135
Clebopride	CYP2D6	0.11	AD	48
Lidoflazine	SLC29A1	1.14	Colorectal Carcinoma	136
	KCNH2	0.19	Short QT syndrome	54
	SCN3A	0.27	Epilepsies	137
	CYP2D6	0.03	AD	48
Fipexide	CYP2D6	0.03	AD	48
	CYP3A4	0.02	AD	57
	CYP1A2	0.03	Liver carcinoma	138
	CYP2C19	0.03	Depressive disorder	139
Estradiol cypionate	ESR1	0.16	Breast neoplasm	96
	AR	0.04	Malignant neoplasm	135

Table 5. Pharmacogenomic analysis of donepezil.

astemizole, nalbuphine, quinidine, aripiprazole, fluspirilene, elacridar, sertindole, vernakalant, sarizotan, fipexide and volinanserine exhibited good inhibition constant value on comparison with standard value $80.08 \mu\text{M}^{208}$. The intermolecular energy is the attractive intermolecular forces between particles that tend to draw the particles together and evaluates based on minimum energy values. According to AutoDock, the binding energy is the sum of the intermolecular forces acting upon the receptor-ligand complex²⁰⁹.

$$\Delta G_{\text{binding}} = \Delta G_{\text{vdw}} + \Delta G_{\text{elec}} + \Delta G_{\text{Hbond}} + \Delta G_{\text{desolv}} + \Delta G_{\text{torsional}} \quad (1)$$

Here, ΔG_{gauss} : attractive term for dispersion of two gaussian functions, $\Delta G_{\text{repulsion}}$: square of the distance if closer than a threshold value, ΔG_{Hbond} : ramp function also used for interactions with metal ions, $\Delta G_{\text{hydrophobic}}$: ramp function, ΔG_{tors} : proportional to the number of rotatable bonds.

Drugs	Genes	Interaction score	Disease associations	Refs.
Morphine	PDYN	4.11	AD	140
	SYP	4.11	Mental retardation	141
	OPRD1	0.32	Alcoholic Intoxication	127
	COMT	1.09	Bipolar Disorder	142
	UGT2B7	0.78	Malignant neoplasm	143
	RHBDF2	1.37	Esophageal cancer	144
	OPRM1	0.2	Alcoholic Intoxication	127
	OPRK1	0.23	AD	145
	TAOK3	2.05	Neoplasm Metastasis	146
	PER1	2.05	AD	147
	HMOX2	2.05	AD	148
	LPAR2	1.37	Breast neoplasm	149
	KCNJ6	0.82	Alcoholic Intoxication, Chronic	150
	GRM1	0.82	Schizophrenia	151
	ABCB1	0.09	AD	55
	F2R	0.26	Stomach neoplasm	152
	GCG	0.26	Diabetes Mellitus	153
	ITGAM	0.41	Lupus Erythematosus	154
	NR4A1	0.41	Pancreatic neoplasm	155
	CCR2	0.37	Pulmonary Fibrosis	156
	SLC22A1	0.27	Liver carcinoma	157
CCKBR	0.2	Panic Disorder	158	
CYP2D6	0.01	AD	57	
DRD2	0.02	AD	68	
Codeine	OPRD1	1.22	Alcoholic Intoxication	127
	OPRM1	0.58	Alcoholic Intoxication	127
	OPRK1	0.63	AD	145
	UGT2B7	0.76	Neoplasm urinary bladder	143
	ABCB1	0.13	AD	55
	CYP3A4	0.02	AD	57
	CYP2D6	0.01	AD	57
	AR	0.01	Prostate neoplasm	135
Hyoscyamine	CHRM5	0.99	Schizophrenia	45
Quinine	CYP3A7	1.27	Malignant Neoplasms	159
	SLC29A4	0.64	AD	160
	COP1	1.27	Neoplasms	161
	IL2	0.6	AD	162
	G6PD	0.18	Anemia	163
	ABCB1	0.03	AD	55
	CYP3A4	0.01	AD	57
	CYP2D6	0.01	AD	57
Oxycodone	RHBDF2	4.71	Esophageal cancer	144
	COMT	2.87	Bipolar Disorder	142
	OPRD1	0.65	Alcoholic Intoxication	127
	OPRM1	0.57	Alcoholic Intoxication	127
	OPRK1	0.56	AD	145
	UGT2B7	0.67	Neoplasm of urinary bladder	143
	NR1I3	1.01	Drug-Induced Liver Disease	164
	CYP3A5	0.21	Malignant neoplasm of prostate	165
ABCB1	0.09	AD	55	
Carteolol	ADRB1	3.11	Hypertensive disease	166
	ADRB2	1.61	Asthma	167
Continued				

Drugs	Genes	Interaction score	Disease associations	Refs.
Atropine	GUCA2A	3.54	Carcinogenesis	168
	CHRM5	0.66	Schizophrenia	45
	F2R	0.66	Stomach neoplasm	152
	CHRM2	0.64	AD	46
	CHRM4	0.54	Schizophrenia	44
	CHRM1	0.43	AD	47
	CYP3A5	0.1	Prostate neoplasm	165
	CHRM3	0.37	AD	43
	AR	0.01	Prostate neoplasm	135
Butorphanol	OPRD1	1.54	Alcoholic Intoxication	127
	OPRK1	1.33	AD	145
	OPRM1	0.88	Alcoholic Intoxication	127
	CYP3A4	0.02	AD	57
	CYP1A2	0.03	Liver carcinoma	138
	CYP2C9	0.04	Unipolar Depression	169
	CYP2C19	0.04	Depressive disorder	139
Latanoprost	PTGFR	19.97	Breast Carcinoma	170
	ABCC4	1.46	Malignant neoplasm of prostate	171
	PTGS1	0.64	Hyperalgesia	172
Mycophenolate mofetil	IMPDH2	1.18	Neoplasm Metastasis	173
	ITGB2	1.12	Leukocyte adhesion deficiency type 1	174
	IMPDH1	1.06	Neoplasm Metastasis	173
	CSF2	0.78	Rheumatoid Arthritis	175
	AR	0.01	Prostate neoplasm	135
Naltrexone	OPRD1	1.47	Alcoholic Intoxication	127
	OPRM1	1.35	Alcoholic Intoxication	127
	OPRK1	0.8	AD	145
	GCG	0.99	Diabetes Mellitus	153
	DBH	1.14	dopamine beta hydroxylase deficiency	176
	BAX	0.33	AD	177
Nalbuphine	OPRK1	1.79	AD	145
	OPRM1	1.11	Alcoholic Intoxication	127
	OPRD1	0.98	Alcoholic Intoxication	127
	CYP2D6	0.04	AD	48
	CYP3A4	0.02	AD	57
	CYP1A2	0.04	Liver carcinoma	138
Bimatoprost	PTGFR	14.98	Breast Carcinoma	170
	PTGER3	5.3	Stevens-Johnson Syndrome	178
	PTGER1	3.54	Breast Carcinoma	170
Quinidine	KCNK5	1.68	Balkan Nephropathy	179
	KCNU1	1.68	Diabetes Mellitus	180
	CYP3A7	0.67	Malignant Neoplasms	159
	KCNT1	0.84	Epileptic encephalopathy	181
	KCNK16	0.84	Diabetes Mellitus	182
	SLC29A4	0.34	AD	160
	KCNH5	0.67	Epilepsy	183
	KCNE1	0.67	Long qt syndrome 5	184
	KCNA7	0.42	Familial heart attack	185
	SCN5A	0.41	Brugada Syndrome	186
	KCNH1	0.28	Temple-Baraitser Syndrome	187
	ABCB1	0.04	AD	55
	CYP3A4	0.02	AD	57
	CYP2D6	0.01	AD	48
	CYP2C9	0.02	Unipolar Depression	169
CYP1A2	0.01	Liver carcinoma	138	
CYP2C19	0.01	Depressive disorder	139	
Continued				

Drugs	Genes	Interaction score	Disease associations	Refs.
Buprenorphine	OPRD1	0.88	Alcoholic Intoxication	127
	OPRM1	0.62	Alcoholic Intoxication	127
	OPRK1	0.43	AD	145
	UGT2B7	0.61	Neoplasm of urinary bladder	143
	COMT	0.4	Bipolar Disorder	142
	CYP3A5	0.12	Malignant neoplasm of prostate	165
	CYP3A4	0.02	AD	57
Ezetimibe	NPC1L1	175.04	Diabetes Mellitus	188
	NPSR1	0.38	Asthma	189
Naloxone	OPRD1	1.07	Alcoholic Intoxication	127
	OPRM1	0.89	Alcoholic Intoxication	127
	OPRK1	0.33	AD	145
	GRP	1.65	Head Neoplasms	190
	NTF3	0.72	Schizophrenia	191
	RARA	0.37	Promyelocytic Leukemia	192
	BDNF	0.18	Congenital hypoventilation	193
Oxymorphone	OPRM1	1.03	Alcoholic Intoxication	127
	OPRD1	0.73	Alcoholic Intoxication	127
	NR1H3	2.27	Drug-Induced Liver Disease	164
	CYP2D6	0.03	AD	48
Paclitaxel	STMN1	1.31	Liver carcinoma	194
	SPATA5	1.31	Epilepsy	195
Ethylmorphine	CYP2D6	0.11	AD	48
Etorphine	OPRD1	2.61	Alcoholic Intoxication	127
	OPRM1	1.2	Alcoholic Intoxication	127
	OPRK1	0.95	AD	145
Diprenorphine	OPRD1	2.28	Alcoholic Intoxication	127
	OPRK1	0.48	AD	145
	OPRM1	0.34	Alcoholic Intoxication	127
Dihydromorphine	OPRD1	1.31	Alcoholic Intoxication	127
	OPRK1	0.95	AD	145
	OPRM1	0.68	Alcoholic Intoxication	127
Dexanabinal	GLRA2	1.74	Autistic Disorder	196
	GLRA3	0.83	Autistic Disorder	196
	GLRA1	0.83	Autistic Disorder	196
	CNR1	0.15	AD	74
Tonabersat	HTR1D	2.12	Adenocarcinoma	73
Eliglustat Edivoxetine	UGCG	15.91	Liver Cirrhosis	197
	CYP2D6	0.16	AD	48
Nalorphine	OPRD1	0.33	Alcoholic Intoxication	127
	OPRK1	0.24	AD	145
ORM-12741	OPRM1	0.17	Alcoholic Intoxication	127
	ADRA2C	0.77	Heart failure	198
Bevenopran	OPRM1	1.03	Alcoholic Intoxication	127
Samidorphan	OPRM1	0.34	Alcoholic Intoxication	127
	OPRD1	0.33	Alcoholic Intoxication	127
	OPRK1	0.24	AD	145
Onapristone	PGR	1.14	Endometriosis	199
	NR3C2	0.92	Pseudohypoadosteronism	200
Nalfurafine	NR3C1	0.32	Pseudohypoadosteronism	200
	OPRK1	0.72	AD	145
Oliceridine	OPRM1	0.51	Alcoholic Intoxication	127
Methylsamidorphan	OPRM1	0.51	Alcoholic Intoxication	127
Navoximod	TDO2	7.07	Schizophrenia	201
Rocagla	<u>NFE2L2</u>	0.08	Lung Carcinoma	202
Continued				

Drugs	Genes	Interaction score	Disease associations	Refs.
Volinanserin	HTR2A	0.44	AD	72
	HTR2B	0.31	AD	72
	HTR2C	0.22	AD	72
Nebivolol	ADRB1	1.21	Hypertensive disease	166
	ADRB2	0.23	Asthma	167
	CYP2D6	0.05	AD	48
Vernakalant	CYP2D6	0.11	AD	48
Nalmefene	OPRD1	1.31	Alcoholic Intoxication	127
	OPRK1	0.95	AD	145
	OPRM1	0.34	Alcoholic Intoxication	127

Table 6. Pharmacogenomic analysis of galantamine.

Docking complexes	Docking energy (Kcal/mol)	Ligand efficiency (Δg)	Inhibition constant (μM)	Intermol energy (Kcal/mol)	Total internal (Kcal/mol)	Torsional energy (Kcal/mol)
Morphine	- 6.31	- 0.30	23.72	- 6.91	- 0.39	0.6
Codeine	- 6.60	- 0.30	14.55	- 7.2	- 0.78	0.6
Quinine	- 6.21	- 0.26	28.07	- 7.7	- 1.1	1.49
Darifenacin	- 7.59	- 0.24	2.73	- 9.68	- 2.5	2.09
Atropine	- 5.41	- 0.26	107.92	- 7.2	- 1.12	1.79
Astemizole	- 7.19	- 0.21	5.37	- 9.58	- 1.7	2.39
Nalbuphine	- 6.36	- 0.24	21.81	- 7.85	- 2.35	1.49
Quinidine	- 6.47	- 0.27	17.94	- 7.97	- 1.19	1.49
Tubocurarine	- 8.26	- 0.18	888.7	- 9.45	- 0.86	1.19
Aripiprazole	- 6.48	- 0.22	17.76	- 8.57	- 1.62	2.09
Fluspirilene	- 6.91	- 0.20	8.57	- 9.0	- 2.29	2.09
Elacridar	- 7.72	- 0.18	2.21	- 10.1	- 1.3	2.39
Sertindole	- 7.58	- 0.24	2.76	- 9.08	- 1.3	1.49
Vernakalant	- 5.59	- 0.22	79.57	- 7.98	- 1.96	2.39
Tariquidar	- 8.42	- 0.18	671.0	- 11.7	- 2.42	- 2.42
Sarizotan	- 6.86	- 0.26	9.35	- 8.35	- 2.25	1.49
Fipexide	- 6.35	- 0.26	22.11	- 8.14	- 1.05	- 1.05
Volinanserin	- 5.80	- 0.21	56.06	- 8.19	- 1.69	- 1.69

Table 7. The predicted docking energy values of selected drugs.

Binding pocket and binding interaction analysis

The active binding site is a cavity on the surface or in the interior of a protein that possesses suitable properties for ligand binding⁴⁰. 18 drugs were docked against death domain of MADD and superimposed all docking complexes to check the binding conformations inside the binding pocket. The predicted results showed that all 18 drugs were firmly bind within the active region of MADD however, the binding behavior was deviant with each other's (Fig. 7A, B).

Drug-protein binding interaction is significant parameter to better understand the molecular docking results and to deeply understand the conformational behavior^{210,211}. Top six drug having docking energy greater than - 7.00 kcal/mol were selected to check the binding conformation behavior and druggability behavior of MADD. The best six drug such as darifenacin (- 7.59), astemizole (- 7.19), tubocurarine (- 8.26), elacridar (- 7.72), sertindole (- 7.58) and tariquidar (- 8.42) exhibited good docking energy values (Kcal/mol) and binding interaction profiles. In darifenacin docking, single hydrogen bond was observed with appropriate binding distance. The amino group (NH₂) of darifenacin formed a hydrogen bond with Glu1020 having bond length 2.60 Å within the active region of death domain of MADD structure. Similarly, elacridar and tariquidar also formed hydrogen bonds with Glu1023 having appropriate bond lengths. The nitrogen atom of NH₂ elacridar formed hydrogen bond with Glu1023 having bond length 3.00 Å, whereas tariquidar formed two hydrogen bonds with Glu1023 having bond distances 2.50 and 2.80 Å, respectively. Glutamic acid is an α -amino acid that is used by almost all living beings in the biosynthesis of proteins. Our docking results showed that screened drugs bind with Glu1020 and Glu1023 which may depict their significance in death domain formation and their involvement in the associated signaling pathways. The reported data showed that hydrogen bond between 2.5 and 3.0 Å may considered as standard bond length in ligand docking which strengthen the docked complexes²¹².

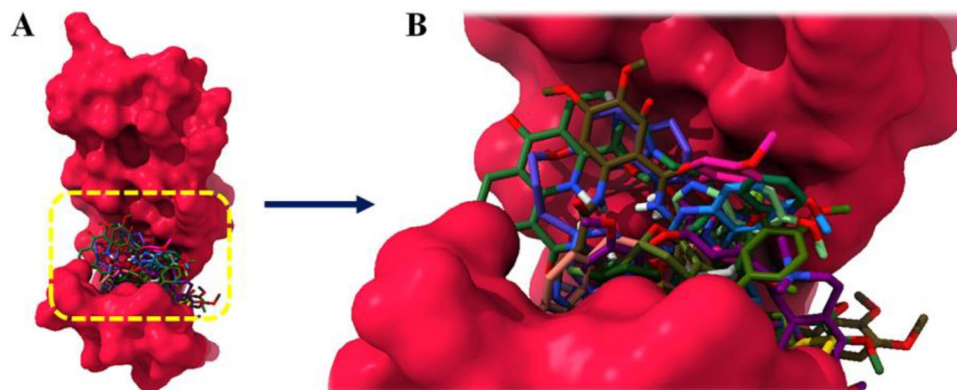


Figure 7. (A) Binding pocket of death domain of MADD protein along with all selected drugs. (B) In detail description, binding of morphine, codeine, quinine, darifenacin, astemizole, nalbuphine, quinidine, aripiprazole, fluspirilene, elacridar, sertindole, vernakalant, sarizotan, fipexide and volinanserin at the active site of target protein.

Therefore, intermolecular hydrogen bonds have good impact in the formation of drug-protein docking complex and enhance their accuracy. In all our docking analysis, darifenacin, elacridar and tariquidar exhibited comparative hydrogen bond length against the MADD protein. The comparative analysis showed that all drugs, darifenacin, astemizole, tubocurarine, elacridar, sertindole and tariquidar were bind at same position inside the active region of death domain in MADD protein. The common interactions pattern among unique residues also showed the reliability of our docking results. Furthermore, in detail results, darifenacin is surrounded by Glu1020, Tyr1008, Ile1005, Met1004, Gln999, Met997 and Glu1023 residues, whereas elacridar and tariquidar also encompassed similar amino acids such as Leu1027, Leu1030, Met1004, Leu1009, Tyr1008, Glu1020, His1060, and Glu1023, respectively. The other three drugs also showed their binding potential at the same binding regions with different conformational symmetry. The occurrence of common amino acids in all docking complexes also ensure the significance of these amino acid particularly Glu1023 is essential for target binding (Fig. 8).

Molecular dynamic simulation

The best docking complexes were analyzed further through the evaluation of residual flexibility in the target protein by employing MD simulation experiment. The MD simulation study was employed at 100 ns by using Gromacs 5.1.2 by generating root mean square deviations & fluctuations (RMSD/F), radius of gyration (Rg) and solvent accessible surface area (SASA) graphs.

Root mean square deviation and fluctuation analysis

The protein backbone behavior in the simulation running time were evaluated through RMSD/F graphs. The RMSD graph results of six docking complexes (darifenacin, astemizole, tubocurarine, elacridar, sertindole and tariquidar) showed the steady and little fluctuated behavior through-out the simulation time. The RMSD graph lines displayed an increasing trend with RMSD values ranging from 0 to 0.1 nm from 0 to 100 ns.

Initially, all the graph lines (red, indigo, brown, green, blue, and yellow) of docked complexes showed an increasing trend with RMSD value 0–0.1 nm from 0 to 10 ns. However, in the same simulation time tariquidar graph line showed much stable behavior as compared to other complexes. From 10 to 20 ns, again fluctuated graphs lines were seen whereas, tariquidar (yellow) remained steady and stable at RMSD value around 0.6 nm. Tubocurarine (brown) displayed highest RMSD value (> 1 nm) at 20 ns as compared to all other graphs lines. Sertindole (blue) line showed upward movement from 0 to 10 ns whereas, from 10 to 20 ns the graph line showed downward movement. However, darifenacin and tubocurarine has been exposed in continuously increasing trend with increased RMSD values (nm). Elacridar (green) and astemizole also showed fluctuated behavior at this simulation time frame. From 20 to 40 ns much stable behavior has been observed in the tariquidar (yellow) and elacridar (green) graphs lines, respectively compared to other graph lines. Darifenacin (red), astemizole (indigo), tubocurarine (brown), elacridar (green), and sertindole (blue) showed high fluctuations in graph lines along with deviated RMSD values.

From 40 to 100 ns, again tariquidar (yellow) remained displayed stable behavior and no fluctuations has been observed in the backbone of MADD protein in the docking complex. Similarly, elacridar (green) also represented similar results with tariquidar and still remained stable behavior in the docking complex. The rest of all other docking complexes showed little fluctuations with steady stable behavior in the simulation time. The RMSD is used to measure the difference between the backbones of a protein from its initial structural conformation to its final position²¹³ and multiple research data exposed different RMSD values range from 0 to 0.3 nm in their MD simulation analysis²⁰³. The overall RMSD graphs lines showed that all docked complexes showed fluctuated behavior in the simulation time frame. The generated graphs results showed the stable behavior in the backbone of all protein complexes (Fig. 9).

The RMSF results of all docked complexes dynamically fluctuated from residues N to C terminals. The protein structures are composed of with different structural architecture. There are different small fluctuations

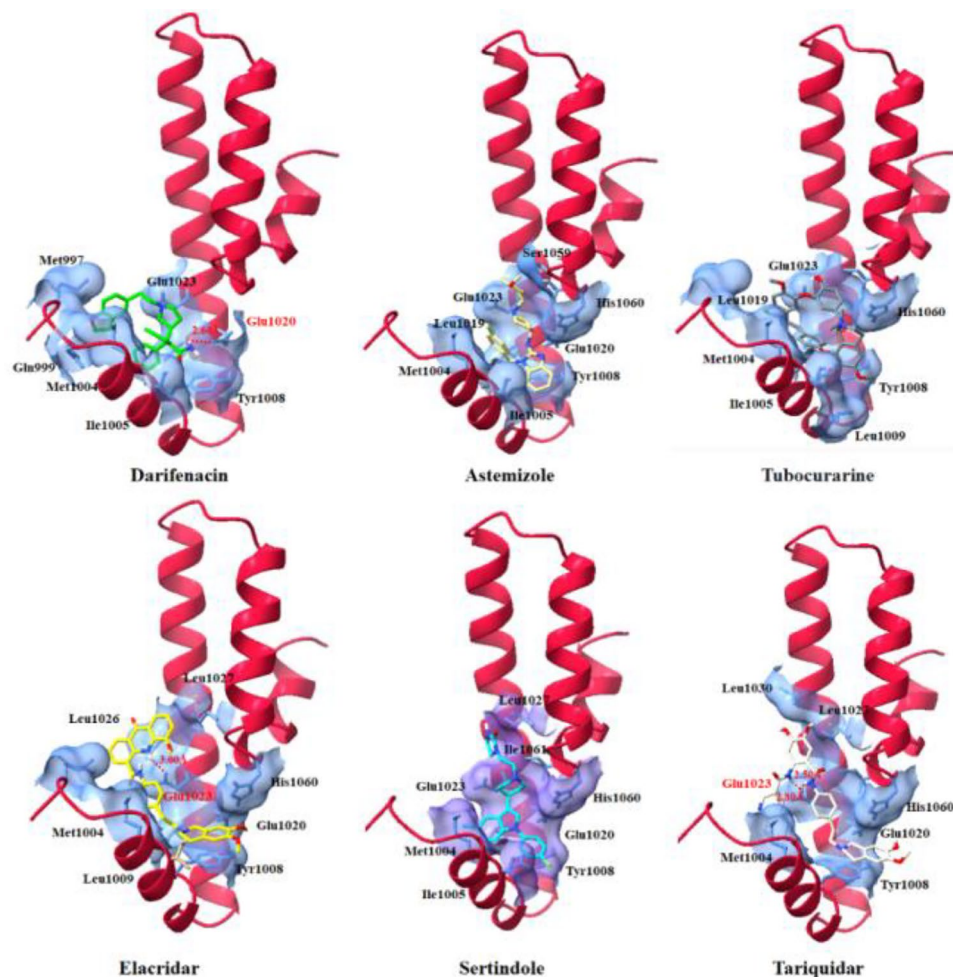


Figure 8. Binding interaction of best darifenacin, astemizole, tubocurarine, elacridar, sertindole and tariquidar death domain of MADD protein along with all selected drug binding.

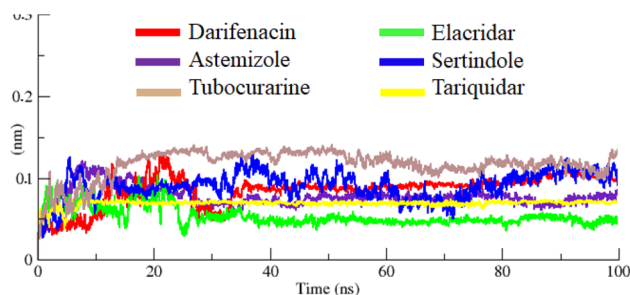


Figure 9. RMSD graph of docked complexes of darifenacin, astemizole, tubocurarine, elacridar, sertindole and tariquidar, respectively from 0 to 100 ns.

through-out the simulation time frame. However, most of protein complexes remain little stable in the RMSF graph. The tariquidar graph line displayed less fluctuations as compared to all other protein complexes which ensure his stable behavior in the docking complex. The comparative results showed that tubocurarine and sertindole were exhibited higher fluctuations peaks, however, the values remain at 0.1 nm in the simulation study. All the results have been displayed in Fig. 10.

Radius of gyration and solvent accessible surface area

The structural compactness of protein was calculated by Rg. The generated results depicted that Rg values of all the docked structures showed little variations from 1.25 to 2.25 nm. Initially, the graph lines were unstable and showed little fluctuations from 0 to 20 ns. The comparative analysis showed that sertindole graph line displayed

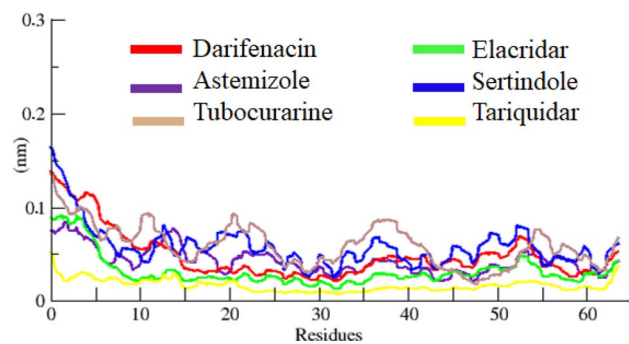


Figure 10. RMSF graph of darifenacin, astemizole, tubocurarine, elacridar, sertindole and tariquidar docking complexes at 100 ns.

fluctuations from 0 to 100 ns. However, darifenacin, astemizole, tubocurarine, elacridar, and tariquidar graph lines were remained stable with less fluctuations after 20–100 ns. The overall stable behavior was observed at the Rg value 1.5 nm (Fig. 11). The solvent-accessible surface areas (SASA) were also observed and shown in. Results showed that the values of SASA of all five docked complexes were centered on 45 nm² in the simulation time 0–100 ns (Fig. 12).

Protein–ligand interaction energy

The interaction energy has been calculated from MD trajectories in couple of forms: electrostatic (coulombic) interaction energy and Lennard–Jones interaction energy, with their sum representing the total interaction energy. According to interaction energy analysis tariquidar drug showed the lowest interaction energy – 285.728 followed by elacridar and tubocurarine (– 248.6337 and – 160.0039 respectively). Moreover, the astemizole, sertindole, and darifenacin exhibit high interaction energy as compared to the top (Table 8). Furthermore, the

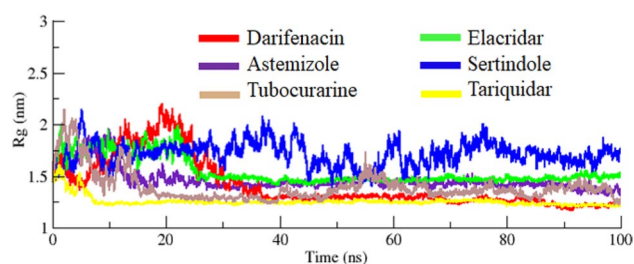


Figure 11. Rg graph of darifenacin, astemizole, tubocurarine, elacridar, sertindole and tariquidar docking complexes from simulation time 0–100 ns.

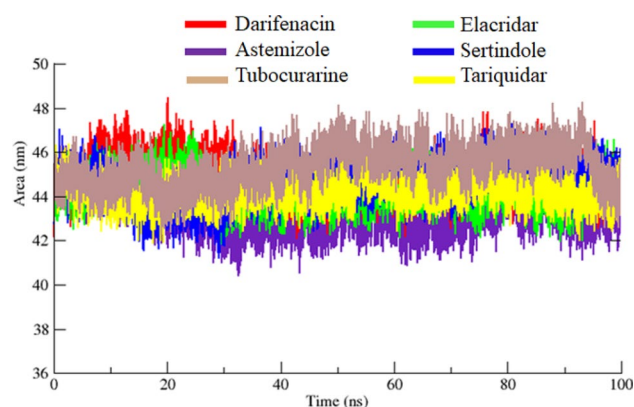


Figure 12. SASA graph of darifenacin, astemizole, tubocurarine, elacridar, sertindole and tariquidar docking structures from 0 to 100 ns simulation time frame.

Drugs	Interaction energy		Total interaction energy
	Coulombic	Lennard-Jones	
Astemizole	- 18.1286	- 116.472	- 134.6006
Darifenacin	- 10.208	- 93.7889	- 103.9969
Elacridar	- 59.3197	- 189.314	- 248.6337
Sertindole	- 11.7399	- 112.683	- 124.4229
Tariquidar	- 101.295	- 184.433	- 285.728
Tobucorarine	- 24.7449	- 135.259	- 160.0039

Table 8. MD protein–ligand Interaction energy table of all six compounds.

graphical depiction of interaction energy of those six drugs has been carried out to see the trajectory changes of all six drugs throughout 100 ns MD simulation (Fig. 13).

Binding poses validation

To analyze the interaction of darifenacin, astemizole, tubocurarine, elacridar, sertindole and tariquidar during 100 ns MD simulation; MD binding Pose validation has been carried out against best selected drugs. Snapshots of all simulated drugs results demonstrated that all drugs remained in the active region of MADD during the 100 ns MD simulation and maintained strong interactions with binding pocket residues. The elacridar manifest the strongest interaction while tubocurarine and sertindole also exhibit single hydrogen bonds and in addition to hydrophobic interactions. Furthermore, astemizole, darifenacin, and tariquidar also exhibits strong hydrophobic interactions. The results demonstrate that the drugs remain bounded to the active pocket of the target protein till 100 ns and block the active site residues (Supplementary Fig. S6).

Conclusion

Novel drug development is time consuming process with relatively high debilitating cost. In present time, drug repositioning is an in-silico approach being employing for drug discovery. In the present research repositioning profiles of known drugs against AD has been explored using shape-based screening, molecular docking pharmacogenomics and MD simulation approaches. Swiss-Similarity results showed 282 drugs were retrieved with donepezil and 351 against galantamine and further evaluated based on similarity scoring values, docking energy values and pharmacogenomics analysis. The detailed pharmacogenomics and extensive data mining showed that three drugs have direct association with AD by targeting different genes. The detailed screening results, showed that darifenacin, astemizole, tubocurarine, elacridar, sertindole and tariquidar drugs exhibited good lead like behavior against AD. Moreover, in MD simulation result tariquidar displayed better stability behavior as compared to rest of other docking complexes drugs with respect to their RMSD, RMSE, SASA and Rg evaluations graphs. Taken together, it has been concluded that tariquidar predicted exhibited better repositioning profiles as compared to other screened FDA approved drugs and may be use in the treatment of AD after in-vitro and clinical assessment in future.

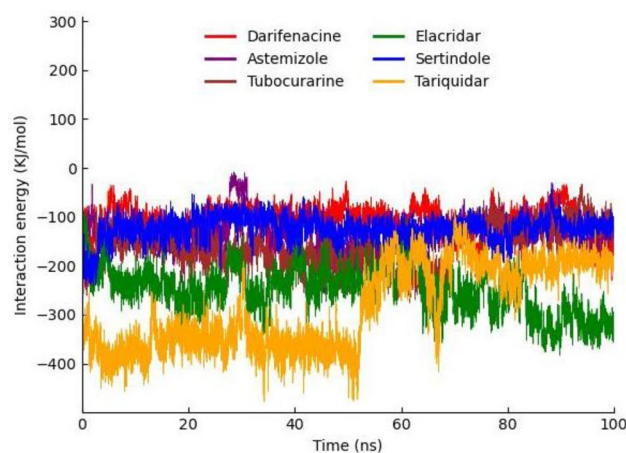


Figure 13. Graphical representation of MD protein–ligand Interaction energy trajectories darifenacin, astemizole, tubocurarine, elacridar, sertindole and tariquidar.

Data availability

The data used or analyzed in the current study are available at different online resources including <https://www.uniprot.org/uniprot/Q8WVG6>; <https://go.drugbank.com/>; <https://www.dgidb.org/>; and <http://dsigdb.tanlab.org/DSigDBv1.0/>, respectively. All the relevant data has been mentioned in the manuscript whereas, rest of supporting information along with dataset names and accession numbers have been mentioned in the supplementary file.

Received: 24 March 2023; Accepted: 18 October 2023

Published online: 21 October 2023

References

- Acarin, L., González, B. & Castellano, B. Stat3 and NF κ B glial expression after excitotoxic damage to the postnatal brain. *NeuroReport* **9**, 2869–2873 (1998).
- Moustafa, A. A. *et al.* Genetic underpinnings in Alzheimer's disease—a review. *Rev. Neurosci.* **29**, 21–38 (2018).
- Cutsuridis, V. & Moustafa, A. A. Neurocomputational models of Alzheimer's disease. *Scholarpedia* **12**, 32144 (2017).
- Ahn, K. S. & Aggarwal, B. B. Transcription factor NF- κ B: A sensor for smoke and stress signals. *Ann. N. Y. Acad. Sci.* **1056**, 218–233 (2005).
- Hassan, M., Raza, H., Abbasi, M. A., Moustafa, A. A. & Seo, S.-Y. The exploration of novel Alzheimer's therapeutic agents from the pool of FDA approved medicines using drug repositioning, enzyme inhibition and kinetic mechanism approaches. *Biomed. Pharmacother.* **109**, 2513–2526 (2019).
- Hawari, F. I. *et al.* Release of full-length 55-kDa TNF receptor 1 in exosome-like vesicles: A mechanism for generation of soluble cytokine receptors. *Proc. Natl. Acad. Sci.* **101**, 1297–1302 (2004).
- Jupp, O. J. *et al.* Type II tumour necrosis factor- α receptor (TNFR2) activates c-Jun N-terminal kinase (JNK) but not mitogen-activated protein kinase (MAPK) or p38 MAPK pathways. *Biochem. J.* **359**, 525–535 (2001).
- Albensi, B. C. & Mattson, M. P. Evidence for the involvement of TNF and NF- κ B in hippocampal synaptic plasticity. *Synapse* **35**, 151–159 (2000).
- Amodio, R. *et al.* Caffeic acid phenethyl ester blocks apoptosis induced by low potassium in cerebellar granule cells. *Int. J. Dev. Neurosci.* **21**, 379–389 (2003).
- Angelo, M. F. *et al.* The proinflammatory RAGE/NF- κ B pathway is involved in neuronal damage and reactive gliosis in a model of sleep apnea by intermittent hypoxia. *PLoS One* **9**, e107901 (2014).
- Miyoshi, J. & Takai, Y. Dual role of DENN/MADD (Rab3GEP) in neurotransmission and neuroprotection. *Trends Mol. Med.* **10**, 476–480 (2004).
- Hassan, M., Zahid, S., Alashwal, H., Kloczkowski, A. & Moustafa, A. A. Mechanistic insights into TNFR1/MADD death domains in Alzheimer's disease through conformational molecular dynamic analysis. *Sci. Reports* **11**, 1–15 (2021).
- Schneider, M., Consortium, T. U. & Poux, S. UniProtKB amid the turmoil of plant proteomics research. *Front. Plant Sci.* **3**, 270 (2012).
- Berman, H. M. *et al.* The protein data bank. *Nucl. Acids Res.* **28**, 235–242 (2000).
- Zhou, X., Hu, J., Zhang, C., Zhang, G. & Zhang, Y. Assembling multidomain protein structures through analogous global structural alignments. *Proc. Natl. Acad. Sci.* **116**, 15930–15938 (2019).
- Gasteiger, E. *et al.* Protein identification and analysis tools on the EXPASY server. In *The Proteomics Protocols Handbook* 571–607 (2005).
- Willard, L. *et al.* VADAR: A web server for quantitative evaluation of protein structure quality. *Nucl. Acids Res.* **31**, 3316–3319 (2003).
- Tosatto, S. C. The victor/FRST function for model quality estimation. *J. Comput. Biol.* **12**, 1316–1327 (2005).
- Studio, D. Discovery studio. *Accelrys [2.1]*. <https://www.3ds.com/products-services/biovia/products/molecular-modeling-simulation/biovia-discoverystudio/> (2008).
- Pettersen, E. F. *et al.* UCSF ChimeraX: Structure visualization for researchers, educators, and developers. *Protein Sci.* **30**, 70–82 (2021).
- Aguirre-Plans, J. *et al.* SPSServer: Split-statistical potentials for the analysis of protein structures and protein–protein interactions. *BMC Bioinform.* **22**, 1–13 (2021).
- Bragina, M. E., Daina, A., Perez, M. A., Michielin, O. & Zoete, V. The SwissSimilarity 2021 web tool: Novel chemical libraries and additional methods for an enhanced ligand-based virtual screening experience. *Int. J. Mol. Sci.* **23**, 811 (2022).
- Cacabelos, R. Donepezil in Alzheimer's disease: From conventional trials to pharmacogenetics. *Neuropsychiatr. Dis. Treat.* **2007**, 896 (2007).
- Razay, G. & Wilcock, G. K. Galantamine in Alzheimer's disease. *Expert Rev. Neurotherapeut.* **8**, 9–17 (2008).
- Jendele, L., Krivak, R., Skoda, P., Novotny, M. & Hoksza, D. PrankWeb: A web server for ligand binding site prediction and visualization. *Nucl. Acids Res.* **47**, W345–W349 (2019).
- Dallakyan, S. & Olson, A. J. *Chemical Biology* 243–250 (Springer, 2015).
- Morris, G. M. *et al.* AutoDock4 and AutoDockTools4: Automated docking with selective receptor flexibility. *J. Comput. Chem.* **30**, 2785–2791 (2009).
- Morris, G. M. *et al.* Automated docking using a Lamarckian genetic algorithm and an empirical binding free energy function. *J. Comput. Chem.* **19**, 1639–1662 (1998).
- Pronk, S. *et al.* GROMACS 4.5: A high-throughput and highly parallel open source molecular simulation toolkit. *Bioinformatics* **29**, 845–854 (2013).
- Chiu, S.-W., Pandit, S. A., Scott, H. & Jakobsson, E. An improved united atom force field for simulation of mixed lipid bilayers. *J. Phys. Chem. B* **113**, 2748–2763 (2009).
- Wang, H., Dommert, F. & Holm, C. Optimizing working parameters of the smooth particle mesh Ewald algorithm in terms of accuracy and efficiency. *J. Chem. Phys.* **133**, 034117 (2010).
- Amiri, S., Sansom, M. S. & Biggin, P. C. Molecular dynamics studies of AChBP with nicotine and carbamylcholine: The role of water in the binding pocket. *Protein Eng. Design Sel.* **20**, 353–359 (2007).
- Bjellqvist, B. *et al.* Micropreparative two-dimensional electrophoresis allowing the separation of samples containing milligram amounts of proteins. *Electrophoresis* **14**, 1375–1378 (1993).
- Xiong, X. *et al.* Enrichment and proteomic analysis of plasma membrane from rat dorsal root ganglions. *Proteome Sci.* **7**, 1–10 (2009).
- Chow, V. T., Lim, K. & Lim, D. The human DENN gene: Genomic organization, alternative splicing, and localization to chromosome 11p11.21-p11.22. *Genome* **41**, 543–552 (1998).
- Heo, L., Park, H. & Seok, C. GalaxyRefine: Protein structure refinement driven by side-chain repacking. *Nucl. Acids Res.* **41**, W384–W388 (2013).

37. Samudrala, R. & Moul, J. An all-atom distance-dependent conditional probability discriminatory function for protein structure prediction. *J. Mol. Biol.* **275**, 895–916 (1998).
38. Jones, D. T. GenTHREADER: An efficient and reliable protein fold recognition method for genomic sequences. *J. Mol. Biol.* **287**, 797–815 (1999).
39. Ramachandran, G. Protein structure and crystallography. *Science* **141**, 288–291 (1963).
40. Stank, A., Kokh, D. B., Fuller, J. C. & Wade, R. C. Protein binding pocket dynamics. *Accounts Chem. Res.* **49**, 809–815 (2016).
41. Krivák, R. & Hoksza, D. In *International Conference on Algorithms for Computational Biology* 41–52 (Springer, 2022).
42. March-Vila, E. *et al.* On the integration of in silico drug design methods for drug repurposing. *Front. Pharmacol.* **8**, 298 (2017).
43. Aulston, B. *et al.* Extracellular vesicles isolated from familial Alzheimer's disease neuronal cultures induce aberrant tau phosphorylation in the wild-type mouse brain. *J. Alzheim. Dis.* **72**, 575–585 (2019).
44. Levrán, O. *et al.* African-specific variability in the acetylcholine muscarinic receptor M4: Association with cocaine and heroin addiction. *Pharmacogenomics* **17**, 995–1003 (2016).
45. De Luca, V. *et al.* Linkage of M5 muscarinic and $\alpha 7$ -nicotinic receptor genes on 15q13 to schizophrenia. *Neuropsychobiology* **50**, 124–127 (2004).
46. Tsang, S. *et al.* Loss of [3H] 4-DAMP binding to muscarinic receptors in the orbitofrontal cortex of Alzheimer's disease patients with psychosis. *Psychopharmacology* **198**, 251–259 (2008).
47. Bradley, S. J. *et al.* M1 muscarinic allosteric modulators slow prion neurodegeneration and restore memory loss. *J. Clin. Investig.* **127**, 487–499 (2017).
48. Chen, X. *et al.* The CYP2D6B allele is associated with a milder synaptic pathology in Alzheimer's disease. *Ann. Neurol.* **38**, 653–658 (1995).
49. Griffiths, S. *et al.* EED and EZH2 constitutive variants: A study to expand the Cohen-Gibson syndrome phenotype and contrast it with Weaver syndrome. *Am. J. Med. Genet. Part A* **179**, 588–594 (2019).
50. Chu, J. T. Histamine H1 receptor gene polymorphism acts as a biological indicator of the prediction of therapeutic efficacy in patients with allergic rhinitis in the Chinese Han population. *J. Cell. Biochem.* **120**, 164–170 (2019).
51. Yan, H. *et al.* CYP2J2 rs890293 polymorphism is associated with susceptibility to Alzheimer's disease in the Chinese Han population. *Neurosci. Lett.* **593**, 56–60 (2015).
52. Fukai, R. *et al.* De novo KCNH1 mutations in four patients with syndromic developmental delay, hypotonia and seizures. *J. Hum. Genet.* **61**, 381–387 (2016).
53. Wang, F. *et al.* Heparanase protects the heart against chemical or ischemia/reperfusion injury. *J. Mol. Cell. Cardiol.* **131**, 29–40 (2019).
54. Hong, K., Bjerregaard, P., Gussak, I. & Brugada, R. Short QT syndrome and atrial fibrillation caused by mutation in KCNH2. *J. Cardiovasc. Electrophysiol.* **16**, 394–396 (2005).
55. Ali, I., Guidone, D., Nicolazzo, J. A. & Brouwer, K. L. Impact of reduced P-glycoprotein function on digoxin concentrations in patients with dementia. *Br. J. Clin. Pharmacol.* **85**, 2351–2359 (2019).
56. Altinoz, M. A. & Ozpınar, A. PPAR- δ and erucic acid in multiple sclerosis and Alzheimer's disease. Likely benefits in terms of immunity and metabolism. *Int. Immunopharmacol.* **69**, 245–256 (2019).
57. Ma, S. L. *et al.* Effect of CYP2D6 and CYP3A4 genotypes on the efficacy of cholinesterase inhibitors in Southern Chinese patients with Alzheimer's disease. *Am. J. Alzheim. Dis. Other Dement.* **34**, 302–307 (2019).
58. Trumbore, C. N. Shear-induced amyloid formation of IDPs in the brain. *Progress Mol. Biol. Transl. Sci.* **166**, 225–309 (2019).
59. Burrage, L. C. *et al.* De novo GMNN mutations cause autosomal-dominant primordial dwarfism associated with Meier-Gorlin syndrome. *Am. J. Hum. Genet.* **97**, 904–913 (2015).
60. Yan, X.-S. *et al.* Protective mechanism of testosterone on cognitive impairment in a rat model of Alzheimer's disease. *Neural Regener. Res.* **14**, 649 (2019).
61. Amor-Gutiérrez, O. *et al.* Competitive electrochemical immunosensor for the detection of unfolded p53 protein in blood as biomarker for Alzheimer's disease. *Analy. Chim. Acta* **1093**, 28–34 (2020).
62. Cai, F. *et al.* A novel mutation of Aryl hydrocarbon receptor interacting protein gene associated with familial isolated pituitary adenoma mediates tumor invasion and growth hormone hypersecretion. *World Neurosurg.* **123**, e45–e59 (2019).
63. Marioni, R. E. *et al.* GWAS on family history of Alzheimer's disease. *Transl. Psychiatry* **8**, 1–7 (2018).
64. Herold, C. *et al.* Family-based association analyses of imputed genotypes reveal genome-wide significant association of Alzheimer's disease with OSBPL6, PTPRG, and PDCL3. *Mol. Psychiatry* **21**, 1608–1612 (2016).
65. Liu, Z.-H. *et al.* Whole-exome mutational and transcriptional landscapes of combined hepatocellular cholangiocarcinoma and intrahepatic cholangiocarcinoma reveal molecular diversity. *Biochim. Biophys. Acta BBA Mol. Basis Dis.* **1864**, 2360–2368 (2018).
66. Lv, H. *et al.* Genome-wide haplotype association study identify the FGFR2 gene as a risk gene for acute myeloid leukemia. *Oncotarget* **8**, 7891 (2017).
67. Pae, C. U., Drago, A., Forlani, M., Patkar, A. A. & Serretti, A. Investigation of an epistatic effect between a set of TAAR6 and HSP-70 genes variations and major mood disorders. *Am. J. Med. Genet. Part B: Neuropsychiatr. Genet.* **153**, 680–683 (2010).
68. Lee, S. H. *et al.* The association of DRD2–141C and ANKK1 Taq1A polymorphisms with alcohol dependence in Korean population classified by the Lesch typology. *Alcohol Alcohol.* **48**, 426–432 (2013).
69. Shrueter, A. & Offen, D. Targeting neurogenesis ameliorates danger assessment in a mouse model of Alzheimer's disease. *Behav. Brain Res.* **261**, 193–201 (2014).
70. Iepsen, E. W. *et al.* Adults with pathogenic MC4R mutations have increased final height and thereby increased bone mass. *J. Bone Miner. Metabol.* **38**, 117–125 (2020).
71. Shen, Y. *et al.* SH2B1 is involved in the accumulation of amyloid- β 42 in Alzheimer's disease. *J. Alzheim. Dis.* **55**, 835–847 (2017).
72. Badamasi, I. M., Lye, M. S., Ibrahim, N. & Stanslas, J. Genetic endophenotypes for insomnia of major depressive disorder and treatment-induced insomnia. *J. Neural Transm.* **126**, 711–722 (2019).
73. Zeng, C. & Chen, Y. HTR1D, TIMP1, SERPINE1, MMP3 and CNR2 affect the survival of patients with colon adenocarcinoma. *Oncol. Lett.* **18**, 2448–2454 (2019).
74. Stumm, C. *et al.* Cannabinoid receptor 1 deficiency in a mouse model of Alzheimer's disease leads to enhanced cognitive impairment despite of a reduction in amyloid deposition. *Neurobiol. Aging* **34**, 2574–2584 (2013).
75. Aparicio, N. *et al.* Role of interleukin 1-beta in the inflammatory response in a fatty acid amide hydrolase-knockout mouse model of Alzheimer's disease. *Biochem. Pharmacol.* **157**, 202–209 (2018).
76. Tajeddinn, W. *et al.* 5-HT1B and other related serotonergic proteins are altered in APPsw mutation. *Neurosci. Lett.* **594**, 137–143 (2015).
77. Li, T. & Zhu, J. Entanglement of CCR5 and Alzheimer's Disease. *Front. Aging Neurosci.* **11**, 209 (2019).
78. Duran-Aniotz, C. *et al.* IRE1 signaling exacerbates Alzheimer's disease pathogenesis. *Acta Neuropathol.* **134**, 489–506 (2017).
79. Porcelijn, L. *et al.* Plasma thrombopoietin levels as additional tool in clinical management of thrombocytopenic neonates. *Platelets* **31**, 62–67 (2020).
80. Castro-Giner, F. *et al.* Positionally cloned genes and age-specific effects in asthma and atopy: An international population-based cohort study (ECRHS). *Thorax* **65**, 124–131 (2010).
81. Topaloglu, A. K. *et al.* TAC3 and TACR3 mutations in familial hypogonadotropic hypogonadism reveal a key role for Neurokinin B in the central control of reproduction. *Nat. Genet.* **41**, 354–358 (2009).

82. Friedrich, P. *et al.* No association of tachykinin receptor 2 (TACR2) polymorphisms with Alzheimer's disease. *Neurobiol. Aging* **32**, 544–545 (2011).
83. Yan, T. *et al.* NK1 (TACR1) receptor gene 'knockout' mouse phenotype predicts genetic association with ADHD. *J. Psychopharmacol.* **24**, 27–38 (2010).
84. Jha, N. K., Kar, R. & Niranjana, R. ABC transporters in neurological disorders: An important gateway for botanical compounds mediated neuro-therapeutics. *Curr. Top. Med. Chem.* **19**, 795–811 (2019).
85. Mitchell, M. *et al.* Genotype analysis and identification of novel mutations in a multicentre cohort of patients with hereditary factor X deficiency. *Blood Coagul. Fibrinol.* **30**, 34–41 (2019).
86. Amodeo, D. A. *et al.* 5-HT6 receptor agonist EMD386088 impairs behavioral flexibility and working memory. *Behav. Brain Res.* **349**, 8–15 (2018).
87. Liu, T.-C. *et al.* LRRK2 but not ATG16L1 is associated with Paneth cell defect in Japanese Crohn's disease patients. *JCI insight* **2**, 6 (2017).
88. Pizzanelli, C. *et al.* Lack of $\alpha 1b$ -adrenergic receptor protects against epileptic seizures. *Epilepsia* **50**, 59–64 (2009).
89. Plach, M. *et al.* Differential allosteric modulation within dopamine D2R-neurotensin NTS1R and D2R-serotonin 5-HT2AR receptor complexes gives bias to intracellular calcium signalling. *Sci. Rep.* **9**, 1–11 (2019).
90. Roth, B. L., Hanizavareh, S. M. & Blum, A. E. Serotonin receptors represent highly favorable molecular targets for cognitive enhancement in schizophrenia and other disorders. *Psychopharmacology* **174**, 17–24 (2004).
91. Lavigne, J. V. *et al.* Genex environment effects of serotonin transporter, dopamine receptor D4, and monoamine oxidase A genes with contextual and parenting risk factors on symptoms of oppositional defiant disorder, anxiety, and depression in a community sample of 4-year-old children. *Dev. Psychopathol.* **25**, 555–575 (2013).
92. Chang, H.-H. *et al.* The prognostic roles of and correlation between ALK and MYCN protein expression in neuroblastoma. *J. Clin. Pathol.* **73**, 154–161 (2020).
93. Kale, Ş., Korum, A. E., Dündar, E. & Erin, N. HSP90 inhibitor PU-H71 increases radiosensitivity of breast cancer cells metastasized to visceral organs and alters the levels of inflammatory mediators. *Naunyn-Schmiedeberg's Arch. Pharmacol.* **393**, 253–262 (2020).
94. Park, C. *et al.* Clinical application of next-generation sequencing-based panel to BRAF wild-type advanced melanoma identifies key oncogenic alterations and therapeutic strategies. *Mol. Cancer Therapeut.* **19**, 937–944 (2020).
95. Ikonomidis, I. *et al.* Differential effects of inhibition of interleukin 1 and 6 on myocardial, coronary and vascular function. *Clin. Res. Cardiol.* **108**, 1093–1101 (2019).
96. Hawse, J. R. *et al.* Optimized immunohistochemical detection of estrogen receptor beta using two validated monoclonal antibodies confirms its expression in normal and malignant breast tissues. *Breast Cancer Res. Treatment* **179**, 241–249 (2020).
97. Dabrowska, M. & Olejniczak, M. *Trinucleotide Repeats* 269–284 (Springer, 2020).
98. Zhou, Y. *et al.* Butein suppresses hepatocellular carcinoma growth via modulating Aurora B kinase activity. *Int. J. Biol. Sci.* **14**, 1521 (2018).
99. Lovinfosse, P. *et al.* Dual time point [18F] FLT-PET for differentiating proliferating tissues vs non-proliferating tissues. *EJNMMI Res.* **9**, 1–8 (2019).
100. Zhang, S. *et al.* Immunohistochemical evaluation of histological change in a Chinese Milroy disease family with venous and skin abnormalities. *Front. Genet.* **10**, 206 (2019).
101. Jinnin, M. *et al.* Suppressed NFAT-dependent VEGFR1 expression and constitutive VEGFR2 signaling in infantile hemangioma. *Nat. Med.* **14**, 1236–1246 (2008).
102. Zhao, L. *et al.* Association study of dopamine receptor genes polymorphism with cognitive functions in bipolar I disorder patients. *J. Affect. Disord.* **170**, 85–90 (2015).
103. Venalis, P. *et al.* Cardiomyopathy in murine models of systemic sclerosis. *Arthritis Rheumatol.* **67**, 508–516 (2015).
104. Bisailon, R. *et al.* Genetic characterization of ABT-199 sensitivity in human AML. *Leukemia* **34**, 63–74 (2020).
105. Hofman, V. *et al.* Multicenter evaluation of a novel ROS1 immunohistochemistry assay (SP384) for detection of ROS1 rearrangements in a large cohort of lung adenocarcinoma patients. *J. Thorac. Oncol.* **14**, 1204–1212 (2019).
106. Rockstroh, D. *et al.* A new p.(Ile66Serfs* 93) IGF2 variant is associated with pre- and postnatal growth retardation. *Eur. J. Endocrinol.* **180**, 1–13 (2019).
107. Chen, X. *et al.* One novel 2.43 Kb deletion and one single nucleotide mutation of the INSR gene in a Chinese neonate with Rabson-Mendenhall syndrome. *J. Clin. Res. Pediatr. Endocrinol.* **10**, 183 (2018).
108. Pierpont, E. I., Semrud-Clikeman, M. & Pierpont, M. E. Variability in clinical and neuropsychological features of individuals with MAP2K1 mutations. *Am. J. Med. Genet. Part A* **173**, 452–459 (2017).
109. Turro, E. *et al.* A dominant gain-of-function mutation in universal tyrosine kinase SRC causes thrombocytopenia, myelofibrosis, bleeding, and bone pathologies. *Sci. Transl. Med.* **8**, 328–330 (2016).
110. Shimony, S. *et al.* Necrotizing hemorrhagic gastritis following acute myeloid leukemia induction with midostaurin: An unexpected complication. *Acta Haematol.* **143**, 65–68 (2020).
111. Tu, H., Zhang, L., Tran, T., Muellemann, R. L. & Li, Y. Diabetes alters protein expression of hyperpolarization-activated cyclic nucleotide-gated channel subunits in rat nodose ganglion cells. *Neuroscience* **165**, 39–52 (2010).
112. Ghafouri-Fard, S., Hafez, A. A. & Taheri, M. Metastasis associated lung adenocarcinoma transcript 1: An update on expression pattern and functions in carcinogenesis. *Exp. Mol. Pathol.* **112**, 104330 (2020).
113. Marini, C. *et al.* HCN1 mutation spectrum: From neonatal epileptic encephalopathy to benign generalized epilepsy and beyond. *Brain* **141**, 3160–3178 (2018).
114. Juang, J.-M. J. & Horie, M. Genetics of Brugada syndrome. *J. Arrhythmia* **32**, 418–425 (2016).
115. Sunderland, P. T. *et al.* 5-Benzamidoisoquinolin-1-ones and 5-(ω -carboxyalkyl) isoquinolin-1-ones as isoform-selective inhibitors of poly (ADP-ribose) polymerase 2 (PARP-2). *J. Med. Chem.* **54**, 2049–2059 (2011).
116. Luan, J., Gao, X., Hu, F., Zhang, Y. & Gou, X. SLFN11 is a general target for enhancing the sensitivity of cancer to chemotherapy (DNA-damaging agents). *J. Drug Target.* **28**, 33–40 (2020).
117. Xiao, G. *et al.* Gain-of-function mutant p53 R273H interacts with replicating DNA and PARP1 in Breast Cancer. Mutant p53 and PARP association with replicating DNA. *Cancer Res.* **80**, 394–405 (2020).
118. Li, H. *et al.* Alcohol consumption, cigarette smoking, and risk of breast cancer for BRCA1 and BRCA2 mutation carriers: Results from the BRCA1 and BRCA2 cohort consortium alcohol and smoking, and breast cancer risk for BRCA carriers. *Cancer Epidemiol. Biomark. Prevent.* **29**, 368–378 (2020).
119. Llorens-Agost, M. *et al.* Analysis of novel missense ATR mutations reveals new splicing defects underlying Seckel syndrome. *Hum. Mut.* **39**, 1847–1853 (2018).
120. Suspitsin, E. *et al.* ATM mutation spectrum in Russian children with ataxia-telangiectasia. *Eur. J. Med. Genet.* **63**, 103630 (2020).
121. Thutkawkorapin, J., Lindblom, A. & Tham, E. Exome sequencing in 51 early onset non-familial CRC cases. *Mol. Genet. Genom. Med.* **7**, e605 (2019).
122. Wang, J. Y., Zhang, X. M. & Zhang, H. Y. The study of thrombospondin-I (TSP1) expression in the early stages of diabetic retinopathy induced by streptozotocin. *J. Mol. Cell Biol.* **39**, 431–437 (2006).

123. Zhang, Z., He, J.-W., Fu, W.-Z., Zhang, C.-Q. & Zhang, Z.-L. Calcification of joints and arteries: Second report with novel NT5E mutations and expansion of the phenotype. *J. Hum. Genet.* **60**, 561–564 (2015).
124. Mazerolles, F. *et al.* Autoimmune lymphoproliferative syndrome-FAS patients have an abnormal regulatory T cell (Treg) phenotype but display normal natural Treg-suppressive function on T cell proliferation. *Front. Immunol.* **9**, 718 (2018).
125. Fan, P. *et al.* Hypertension and brachydactyly syndrome associated with vertebral artery malformation caused by a PDE3A missense mutation. *Am. J. Hypertens.* **33**, 190–197 (2020).
126. Riancho, J. *et al.* Association of ACACB polymorphisms with obesity and diabetes. *Mol. Genet. Metabol.* **104**, 670–676 (2011).
127. Samochowiec, A. *et al.* The role of OPRM1 polymorphism in the etiology of alcoholism. *Adv. Clin. Exp. Med.* **28**, 199–202 (2019).
128. Pan, J. H. *et al.* Nicotinamide phosphoribosyl transferase regulates cell growth via the Sirt1/P53 signaling pathway and is a prognosis marker in colorectal cancer. *J. Cell. Physiol.* **234**, 4385–4395 (2019).
129. Guo, T. A. *et al.* Clinicopathologic features and prognostic value of KRAS, NRAS and BRAF mutations and DNA mismatch repair status: A single-center retrospective study of 1,834 Chinese patients with Stage I-IV colorectal cancer. *Int. J. Cancer* **145**, 1625–1634 (2019).
130. Bellaye, P.-S. *et al.* Synergistic role of HSP90 α and HSP90 β to promote myofibroblast persistence in lung fibrosis. *Eur. Respir. J.* **51**, 2 (2018).
131. Dabral, S. *et al.* A RASSF1A-HIF1 α loop drives Warburg effect in cancer and pulmonary hypertension. *Nat. Commun.* **10**, 1–18 (2019).
132. Majolo, F., Marinowic, D. R., Machado, D. C. & Da Costa, J. C. MTOR pathway in focal cortical dysplasia type 2: What do we know?. *Epilepsy Behav.* **85**, 157–163 (2018).
133. Del Castillo, U. *et al.* Conserved role for Ataxin-2 in mediating endoplasmic reticulum dynamics. *Traffic* **20**, 436–447 (2019).
134. Kostovska, I. M. *et al.* Rare ATAD5 missense variants in breast and ovarian cancer patients. *Cancer Lett.* **376**, 173–177 (2016).
135. Lu, Q. *et al.* Bicalutamide plus aromatase inhibitor in patients with estrogen receptor-positive/androgen receptor-positive advanced breast cancer. *The Oncologist* **25**, 21–e15 (2020).
136. Snezhkina, A. V. *et al.* Differential expression of alternatively spliced transcripts related to energy metabolism in colorectal cancer. *BMC Genom.* **17**, 199–211 (2016).
137. Holland, K. D. *et al.* Mutation of sodium channel SCN3A in a patient with cryptogenic pediatric partial epilepsy. *Neurosci. Lett.* **433**, 65–70 (2008).
138. Wuensch, T. *et al.* Hepatic CYP1A2 activity in liver tumors and the implications for preoperative volume-function analysis. *Am. J. Physiol. Gastrointest. Liver Physiol.* **316**, 608–614 (2019).
139. Jukić, M. M. *et al.* Elevated CYP2C19 expression is associated with depressive symptoms and hippocampal homeostasis impairment. *Mol. Psychiatry* **22**, 1155–1163 (2017).
140. Yakovleva, T. *et al.* Dysregulation of dynorphins in Alzheimer disease. *Neurobiol. Aging* **28**, 1700–1708 (2007).
141. Tarpey, P. S. *et al.* A systematic, large-scale resequencing screen of X-chromosome coding exons in mental retardation. *Nat. Genet.* **41**, 535–543 (2009).
142. Pignoni, A. *et al.* The impact of COMT polymorphisms on cognition in bipolar disorder: A review: Special section on “translational and neuroscience studies in affective disorders” section Editor, Maria Nobile MD, PhD. This Section of JAD focuses on the relevance of translational and neuroscience studies in providing a better understanding of the neural basis of affective disorders. The main aim is to briefly summarize relevant research findings in clinical neuroscience with particular regards to specific innovative topics in mood and anxiety disorders. *J. Affect. Disord.* **243**, 545–551 (2019).
143. Cui, X. *et al.* Association of genotypes of carcinogen-metabolizing enzymes and smoking status with bladder cancer in a Japanese population. *Env. Health Prevent. Med.* **18**, 136–142 (2013).
144. Saarinen, S. *et al.* Analysis of a Finnish family confirms RHBDF2 mutations as the underlying factor in tylosis with esophageal cancer. *Fam. Cancer* **11**, 525–528 (2012).
145. Li, S. *et al.* Development and in vivo evaluation of a κ -opioid receptor agonist as a PET radiotracer with superior imaging characteristics. *J. Nucl. Med.* **60**, 1023–1030 (2019).
146. Bian, Y. *et al.* Target deconvolution of a multikinase inhibitor with antimetastatic properties identifies TAOK3 as a key contributor to a cancer stem cell-like phenotype TAOK3 is a novel target in pancreatic cancer stem cells. *Mol. Cancer Therapeut.* **18**, 2097–2110 (2019).
147. Tseng, J. *et al.* Expression of inducible nitric oxide synthase (iNOS) and period 1 (PER1) clock gene products in different sleep stages of patients with cognitive impairment. *J. Clin. Neurosci.* **17**, 1140–1143 (2010).
148. Shibata, N., Ohnuma, T., Baba, H. & Arai, H. No genetic association between polymorphisms of heme oxygenase 1 and 2 and Alzheimer’s disease in a Japanese population. *Dement. Geriatr. Cogn. Disord.* **27**, 273–277 (2009).
149. Cha, Y. J. & Koo, J. S. Expression of autotaxin-lysophosphatidate signaling-related proteins in breast cancer with adipose stroma. *Int. J. Mol. Sci.* **20**, 2102 (2019).
150. Clarke, T.-K. *et al.* KCNJ6 is associated with adult alcohol dependence and involved in gene \times early life stress interactions in adolescent alcohol drinking. *Neuropsychopharmacology* **36**, 1142–1148 (2011).
151. Ayoub, M. A. *et al.* Deleterious GRM1 mutations in schizophrenia. *PLoS One* **7**, e32849 (2012).
152. Otsuki, T., Fujimoto, D., Hirono, Y., Goi, T. & Yamaguchi, A. Thrombin conducts epithelial-mesenchymal transition via protease-activated receptor-1 in human gastric cancer. *Int. J. Oncol.* **45**, 2287–2294 (2014).
153. El, K. & Campbell, J. E. The role of GIP in α -cells and glucagon secretion. *Peptides* **125**, 170213 (2020).
154. Gupta, V. *et al.* Association of ITGAM, TNFSF4, TNFAIP3 and STAT4 gene polymorphisms with risk of systemic lupus erythematosus in a North Indian population. *Lupus* **27**, 1973–1979 (2018).
155. Lee, H.-S., Safe, S. & Lee, S.-O. Inactivation of the orphan nuclear receptor NR4A1 contributes to apoptosis induction by fangchinoline in pancreatic cancer cells. *Toxicol. Appl. Pharmacol.* **332**, 32–39 (2017).
156. Milger, K. *et al.* Pulmonary CCR2+ CD4+ T cells are immune regulatory and attenuate lung fibrosis development. *Thorax* **72**, 1007–1020 (2017).
157. Herraes, E. *et al.* Expression of SLC22A1 variants may affect the response of hepatocellular carcinoma and cholangiocarcinoma to sorafenib. *Hepatology* **58**, 1065–1073 (2013).
158. Koszycki, D. *et al.* CCK-B receptor gene and response to cholecystokinin-tetrapeptide in healthy volunteers. *Peptides* **35**, 9–13 (2012).
159. Li, H. & Lampe, J. N. Neonatal cytochrome P450 CYP3A7: A comprehensive review of its role in development, disease, and xenobiotic metabolism. *Arch. Biochem. Biophys.* **673**, 108078 (2019).
160. Sekhar, G. N. *et al.* Region-specific blood-brain barrier transporter changes leads to increased sensitivity to amisulpride in Alzheimer’s disease. *Fluids Barriers CNS* **16**, 1–19 (2019).
161. Xie, Y. *et al.* COP1/DET1/ETS axis regulates ERK transcriptome and sensitivity to MAPK inhibitors. *J. Clin. Investig.* **128**, 1442–1457 (2018).
162. Meng, K. *et al.* The effects of vitamin K1 and vitamin K2 on the proliferation, cytokine production and regulatory T-cell frequency in peripheral blood mononuclear cells of paediatric atopic dermatitis patients. *Exp. Dermatol.* **27**, 1058–1060 (2018).
163. Devendra, R. *et al.* A novel G6PD p. Gly 321 Val mutation causing severe Hemolysis in an Indian infant. *Indian J. Hematol. Blood Transf.* **35**, 399–401 (2019).
164. Zimmer, V., Liebe, R. & Lammert, F. Nuclear receptor variants in liver disease. *Digest. Dis.* **33**, 415–419 (2015).

165. Vaarala, M. H. *et al.* The interaction of CYP3A5 polymorphisms along the androgen metabolism pathway in prostate cancer. *Int. J. Cancer* **122**, 2511–2516 (2008).
166. Zhao, Y. *et al.* A new sight for detecting the ADRB1 gene mutation to guide a therapeutic regimen for hypertension based on a CeO₂-doped nanoprobe. *Biosens. Bioelectron.* **92**, 402–409 (2017).
167. Yu, X. *et al.* Correlation study on β 2-adrenergic receptor gene polymorphisms and asthma susceptibility: Evidence based on 57 case-control studies. *Eur. Rev. Med. Pharmacol. Sci.* **23**, 3908–3925 (2019).
168. Weinberg, D. S. *et al.* Bioactivity of oral linaclotide in human colorectum for cancer chemopreventionlinaclotide bioactivity in human colorectum. *Cancer Prevent. Res.* **10**, 345–354 (2017).
169. Ruaño, G. *et al.* Physiogenomic analysis of CYP450 drug metabolism correlates dyslipidemia with pharmacogenetic functional status in psychiatric patients. *Biomark. Med.* **5**, 439–449 (2011).
170. Sossey-Alaoui, K., Kitamura, E. & Cowell, J. K. Fine mapping of the PTGFR gene to 1p31 region and mutation analysis in human breast cancer. *Int. J. Mol. Med.* **7**, 543–546 (2001).
171. Bawa, P. S., Ravi, S., Paul, S., Chaudhary, B. & Srinivasan, S. A novel molecular mechanism for a long non-coding RNA PCAT92 implicated in prostate cancer. *Oncotarget* **9**, 32419 (2018).
172. Kumari, P., Kaur, S., Kaur, J., Bhatti, R. & Singh, P. Modification of the lead molecule: Tryptophan and piperidine appended triazines reversing inflammation and hyperalgesia in rats. *Bioorg. Med. Chem.* **28**, 115246 (2020).
173. Duan, S. *et al.* IMPDH2 promotes colorectal cancer progression through activation of the PI3K/AKT/mTOR and PI3K/AKT/FOXO1 signaling pathways. *J. Exp. Clin. Cancer Res.* **37**, 1–16 (2018).
174. Zhang, Y. *et al.* A novel mutation of the ITGB2 gene in a Chinese Zhuang minority patient with leukocyte adhesion deficiency type 1 and glucose-6-phosphate dehydrogenase deficiency. *Gene* **715**, 144027 (2019).
175. Neidhart, M. *et al.* Oligomeric S100A4 is associated with monocyte innate immune memory and bypass of tolerance to subsequent stimulation with lipopolysaccharides. *Front. Immunol.* **10**, 791 (2019).
176. Kim, C.-H. *et al.* Norepinephrine deficiency is caused by combined abnormal mRNA processing and defective protein trafficking of dopamine β -hydroxylase. *J. Biol. Chem.* **286**, 9196–9204 (2011).
177. Liu, Z., Niu, W., Yang, X., Niu, X. & Yuan, W. Effect of “Xiusanzhen” on expression of hippocampal Bcl-2 and Bax proteins in Alzheimer disease rats. *Acupunct. Res.* **36**, 7–11 (2011).
178. Ueta, M. *et al.* Association between prostaglandin E receptor 3 polymorphisms and Stevens-Johnson syndrome identified by means of a genome-wide association study. *J. Allergy Clin. Immunol.* **126**, 1218–1225 (2010).
179. Toncheva, D. *et al.* NGS nominated CELA1, HSPG2, and KCNK5 as candidate genes for predisposition to Balkan endemic nephropathy. *BioMed Res. Int.* **2014**, 785 (2014).
180. Zhao, W. *et al.* Identification of new susceptibility loci for type 2 diabetes and shared etiological pathways with coronary heart disease. *Nat. Genet.* **49**, 1450–1457 (2017).
181. Hamdan, F. F. *et al.* High rate of recurrent de novo mutations in developmental and epileptic encephalopathies. *Am. J. Hum. Genet.* **101**, 664–685 (2017).
182. Permana, S., Lukman, H., Norahmawati, E., Kawamoto, Y. & Endharti, T. East Asian Genome-wide association study derived loci in relation to type 2 diabetes in the Han Chinese population. *Acta Biochim. Polon.* **66**, 679–686 (2019).
183. Veeramah, K. R. *et al.* Exome sequencing reveals new causal mutations in children with epileptic encephalopathies. *Epilepsia* **54**, 1270–1281 (2013).
184. Harmer, S. & Tinker, A. The role of abnormal trafficking of KCNE1 in long QT syndrome 5. *Biochem. Soc. Trans.* **35**, 1074–1076 (2007).
185. Barden-Kruger, S. *et al.* Characterisation of the human voltage-gated potassium channel gene, KCNA7, a candidate gene for inherited cardiac disorders, and its exclusion as cause of progressive familial heart block I (PFHBI). *Eur. J. Hum. Genet.* **10**, 36–43 (2002).
186. Li, X., Liu, N. & Bai, R. Variant frequencies of KCNQ1, KCNH2, and SCN5A in a Chinese inherited arrhythmia cohort and other disease cohorts undergoing genetic testing. *Ann. Hum. Genet.* **84**, 161–168 (2020).
187. Mastrangelo, M. *et al.* Epilepsy in KCNH1-related syndromes. *Epileptic Disord.* **18**, 123–136 (2016).
188. Lally, S., Owens, D. & Tomkin, G. H. Genes that affect cholesterol synthesis, cholesterol absorption, and chylomicron assembly: The relationship between the liver and intestine in control and streptozotocin diabetic rats. *Metabolism* **56**, 430–438 (2007).
189. Hu, W.-P., Zeng, Y.-Y., Zuo, Y.-H. & Zhang, J. Identification of novel candidate genes involved in the progression of emphysema by bioinformatic methods. *Int. J. Chron. Obstruct. Pulmon. Dis.* **13**, 3733 (2018).
190. Zhang, Q. *et al.* SRC family kinases mediate epidermal growth factor receptor ligand cleavage, proliferation, and invasion of head and neck cancer cells. *Cancer Res.* **64**, 6166–6173 (2004).
191. Skibinska, M. *et al.* Correlation of metabolic parameters, neurotrophin-3, and neurotrophin-4 serum levels in women with schizophrenia and first-onset depression. *Nordic J. Psychiatry* **73**, 96–103 (2019).
192. Xiong, L. *et al.* NLS-RAR α contributes to differentiation block and increased leukemogenic potential in vivo. *Cell. Signal.* **65**, 109431 (2020).
193. Weese-Mayer, D. E., Bolk, S., Silvestri, J. M. & Chakravarti, A. Idiopathic congenital central hypoventilation syndrome: Evaluation of brain-derived neurotrophic factor genomic DNA sequence variation. *Am. J. Med. Genet.* **107**, 306–310 (2002).
194. Zhang, R. *et al.* STMN1 upregulation mediates hepatocellular carcinoma and hepatic stellate cell crosstalk to aggravate cancer by triggering the MET pathway. *Cancer Sci.* **111**, 406–417 (2020).
195. Szczaluba, K. *et al.* *Respiratory System Diseases* 59–66 (Springer, 2017).
196. Pilorge, M. *et al.* Genetic and functional analyses demonstrate a role for abnormal glycinergic signaling in autism. *Mol. Psychiatry* **21**, 936–945 (2016).
197. AbdulHameed, M. D. M. *et al.* Systems level analysis and identification of pathways and networks associated with liver fibrosis. *PLoS One* **9**, e112193 (2014).
198. Amir, O. *et al.* Absence of the α 2c-Adrenoceptor Del322–325 allele is associated with increased mortality in patients with chronic systolic heart failure. *J. Cardiac Fail.* **18**, 925–929 (2012).
199. Choi, J., Jo, M., Lee, E., Lee, D.-Y. & Choi, D. Dienogest regulates apoptosis, proliferation, and invasiveness of endometriotic cyst stromal cells via endoplasmic reticulum stress induction. *Mol. Hum. Reprod.* **26**, 30–39 (2020).
200. Riepe, F. G. & Holterhus, P.-M. Exclusion of serum- and glucocorticoid-induced kinase 1 (SGK1) as a candidate gene for genetically heterogeneous renal pseudohypaldosteronism type I in eight families. *Am. J. Nephrol.* **27**, 164–169 (2007).
201. Miller, C. L. *et al.* Two complex genotypes relevant to the kynurenine pathway and melatonin function show association with schizophrenia and bipolar disorder. *Schizophr. Res.* **113**, 259–267 (2009).
202. Jeong, Y. *et al.* Role of KEAP1/NFE2L2 mutations in the chemotherapeutic response of patients with non-small cell lung cancer KEAP1/NFE2L2 mutations in NSCLC. *Clin. Cancer Res.* **26**, 274–281 (2020).
203. Hassan, M., Yasir, M., Shahzadi, S. & Kloczkowski, A. Exploration of potential ewing sarcoma drugs from FDA-approved pharmaceuticals through computational drug repositioning, pharmacogenomics, molecular docking, and MD simulation studies. *ACS Omega* **2022**, 852 (2022).
204. Hassan, M., Ashraf, Z., Abbas, Q., Raza, H. & Seo, S.-Y. Exploration of novel human tyrosinase inhibitors by molecular modeling, docking and simulation studies. *Interdiscipl. Sci. Comput. Life Sci.* **10**, 68–80 (2018).

205. Hassan, M. *et al.* Molecular docking and dynamic simulation of AZD3293 and solanezumab effects against BACE1 to treat Alzheimer's disease. *Front. Comput. Neurosci.* **12**, 34 (2018).
206. Hassan, M. *et al.* Designing of promising medicinal scaffolds for Alzheimer's disease through enzyme inhibition, lead optimization, molecular docking and dynamic simulation approaches. *Bioorg. Chem.* **91**, 103138 (2019).
207. Hopkins, A. L., Groom, C. R. & Alex, A. Ligand efficiency: A useful metric for lead selection. *Drug Discov. Today* **9**, 430–431 (2004).
208. Umamaheswari, M. *et al.* Docking studies: In silico aldose reductase inhibitory activity of commercially available flavonoids. *Banglad. J. Pharmacol.* **7**, 108–113 (2012).
209. Lin, H.-L., Zhang, H., Medower, C., Hollenberg, P. F. & Johnson, W. W. Inactivation of cytochrome P450 (P450) 3A4 but not P450 3A5 by OSI-930, a thiophene-containing anticancer drug. *Drug Metabol. Dispos.* **39**, 345–350 (2011).
210. Tasleem, M., Hussein, W. M., El-Sayed, A.-A.A. & Alrehaily, A. Providencia alcalifaciens—assisted bioremediation of chromium-contaminated groundwater: A computational study. *Water* **15**, 1142 (2023).
211. Tasleem, M. *et al.* Computational analysis of PTP-1B site-directed mutations and their structural binding to potential inhibitors. *Cell. Mol. Biol.* **68**, 75–84 (2022).
212. McRee, D. E. *Practical Protein Crystallography* (Elsevier, 1999).
213. Aier, I., Varadwaj, P. K. & Raj, U. Structural insights into conformational stability of both wild-type and mutant EZH2 receptor. *Sci. Rep.* **6**, 1–10 (2016).

Acknowledgements

A.K. acknowledges financial support from NSF Grant DBI 1661391 and NIH Grants R01GM127701 and R01HG012117. M.H. acknowledges the Ohio State University for providing the “President's Postdoctoral Scholars Program (PPSP)” award and for financial support to complete this computational research.

Author contributions

M.H. designed this study. S S and M.Y collected data and run experiments; M.H. wrote the initial draft of the manuscript; A.K. and W. C edited the manuscript and compiled it into the final format.

Competing interests

The authors declare no competing interests.

Additional information

Supplementary Information The online version contains supplementary material available at <https://doi.org/10.1038/s41598-023-45347-1>.

Correspondence and requests for materials should be addressed to M.H. or A.K.

Reprints and permissions information is available at www.nature.com/reprints.

Publisher's note Springer Nature remains neutral with regard to jurisdictional claims in published maps and institutional affiliations.



Open Access This article is licensed under a Creative Commons Attribution 4.0 International License, which permits use, sharing, adaptation, distribution and reproduction in any medium or format, as long as you give appropriate credit to the original author(s) and the source, provide a link to the Creative Commons licence, and indicate if changes were made. The images or other third party material in this article are included in the article's Creative Commons licence, unless indicated otherwise in a credit line to the material. If material is not included in the article's Creative Commons licence and your intended use is not permitted by statutory regulation or exceeds the permitted use, you will need to obtain permission directly from the copyright holder. To view a copy of this licence, visit <http://creativecommons.org/licenses/by/4.0/>.

© The Author(s) 2023